IEEE Access
Multidisciplinary | Rapid Review | Open Access Journal

Received 11 November 2023, accepted 1 January 2024, date of publication 4 January 2024,
date of current version 10 January 2024.

Digital Object Identifier 10.1109/ACCESS.2024.3349600

RESEARCH ARTICLE

A PPN-Based Improved QAM-FBMC System With Jointly Optimized Mismatched Prototype Filters

TAEJUN JANG AND JOON HO CHO, (Member, IEEE)
Department of Electrical Engineering (EE), Pohang University of Science and Technology (POSTECH), Pohang 37673, South Korea

Corresponding author: Joon Ho Cho (jcho@postech.ac.kr)

This work was supported by the Electronics and Telecommunications Research Institute (ETRI) grant funded by the Information and Communication Technology (ICT) Research and Development Program of the Ministry of Science and ICT (MSIT)/Institute of Information and Communications Technology Planning and Evaluation (IITP) (Development of Adaptive Interference Reduction Technology Based on Civil-Military Shared Frequency Environment) under Grant 2022-0-00024.

ABSTRACT Recently, it is shown that a spectrally-efficient low-complexity quadrature amplitude modulation (QAM) filter-bank multicarrier (FBMC) system can be designed by relaxing the constraints on the time-frequency (TF) product at the transmitter (TX) and the time-domain localization at the receiver (RX). However, it turns out that the attainable signal-to-interference-plus-noise ratio (SINR) is not satisfactory enough to support certain high-order modulations. This is because, given the PHYDYAS TX prototype filter, only the RX filter is optimized under a sparsity constraint. In this paper, we propose an improved QAM-FBMC system to further reduce self-interference by jointly optimizing the TX and RX prototype filters. The sparsity constraint on the RX prototype filter is now removed, and a new polyphase network (PPN)-based structure is introduced to maintain the complexity at the RX to almost the same level. The joint optimization is formulated as an approximate SINR maximization and converted to a line search, under the constraint on the fall-off rate of the TX prototype filter for high spectral confinement. For each search-parameter value which is a lower bound on the post-processing signal-to-noise ratio (SNR), the prototype filters are optimized to maximize the signal-to-interference ratio (SIR). The line search stops at a saturation point of the SINR, and the pair of fixed TX and RX filters obtained at the point is used for all SNR ranges. Numerical results show that the prototype filters combined with the PPN-based structure achieve low self-interference and lead to a spectrally-efficient low-complexity QAM-FBMC system.

INDEX TERMS Bi-orthogonality, polyphase network, prototype filter, QAM-FBMC, spectral efficiency.

I. INTRODUCTION

Orthogonal frequency-division multiplexing (OFDM) is mainly employed as the waveform for the fourth and fifth generation cellular communication as well as the most updated Wi-Fi systems [1], [2], [3]. However, the rectangular-like transmit waveform, together with the cyclic prefix (CP) used to easily remove inter-symbol interference (ISI), not only reduces the spectral efficiency (SE) of the system but also makes the system vulnerable to synchronization error, causing intercarrier interference (ICI) [4], [5], [6], [7].

Filter-bank multicarrier (FBMC) has been considered as one of the promising waveforms for the next generation communication systems, because several shortcomings of OFDM can be well addressed [5], [6], [7], [8], [9]. In particular, unlike offset quadrature amplitude modulation (OQAM)-FBMC, quadrature amplitude modulation (QAM)-FBMC allows direct application of modern coding/decoding schemes and multiple-input multiple-output (MIMO) techniques [10], [11], [12]. However, QAM-FBMC systems inherently face challenges stemming from the Balian-Low theorem [12]. Specifically, the theorem implies that the transmitter (TX) and receiver (RX) prototype filters cannot simultaneously achieve complex (bi-)orthogonality, excellent time-frequency (TF) localization, and a TF symbol density of unity [13].

Most QAM-FBMC systems developed so far have tackled these challenges without relaxing the unit TF symbol density [11], [12], [14], [15], [16], [17], [18], [19], [20], [21], [22], [23]. This leads to inevitable degradation in complex

The associate editor coordinating the review of this manuscript and approving it for publication was Arun Prakash.

(bi-)orthogonality or TF localization and, consequently, increases self-interference or out-of-band emission of the systems. Among these, conventional QAM-FBMC systems that have a frequency-domain (FD) channel equalizer and a fixed matched filter at the RX, struggle to attain both low self-interference and high spectral confinement at the same time [11], [12], [14], [15], [16], [17]. The primary focus in designing these systems has been the design of the prototype filters. Some of the systems employ a pair of alternating prototype filters at the TX and a matched filter at the RX [11], [12], [14], [15]. However, they mostly have relatively high out-of-band emission [11], [12], [14], while the others have high self-interference [15]. In an attempt to enhance spectral confinement, some systems propose the use of a single prototype filter at the TX and a matched filter at the RX [16], [17], which effectively reduces out-of-band emission but self-interference is still comparatively high.

Recent proposals of QAM-FBMC systems feature various structures, moving beyond just the design of prototype filters. These advancements present alternative approaches to enhancing system performance. Recently proposed QAM-FBMC systems, which have a linear minimum mean-squared error (LMMSE) RX that is a type of mismatched filter, achieve an improved self-interference level and the TF localization of the TX filter to a certain extent but suffer from high complexity [18]. To further reduce self-interference, some systems integrate additional iterative interference cancellation (IIC) at the RX, which escalates complexity [19], [20]. Systems using a hexagonal lattice structure are also proposed, but show limited performance improvements, only effective for 4-QAM [22], [23]. Also, systems with shorter filters are proposed by using the overlapping factor of one [20], [21], [22] for low latency specifically.

Unlike these QAM-FBMC systems, there are few systems that attempt to relax the TF symbol density from unity. While a system with halved TF symbol density is discussed in [24], it is deemed impractical due to a significant reduction in spectral efficiency. Systems proposed in [25] slightly relax the TF symbol density. Interestingly, these systems employ a uniquely high overlapping factor of 16 or 32, compared to typical FBMC systems which generally have an overlapping factor of around 4. This large overlapping factor aids in enhancing spectral confinement, and the systems effectively reduce self-interference with the relaxed TF symbol density. They are suitable for multi-user uplink scenarios where each user utilizes a small number of subcarriers. However, using them with a large number of subcarriers becomes challenging due to the increased computational complexity from the large overlapping factor. Additionally, they use a matched filter, leading to limited improvements in self-interference reduction.

Recently, a QAM-FBMC system is proposed that relaxes both the TF symbol density at the TX and the time-domain (TD) localization at the RX [26]. At the TX, this system employs the PHYDYAS filter as the prototype filter, which has excellent spectral confinement [27]. At the RX, unlike the conventional QAM-FBMC systems [11], [12], [14], [16], [18], [19], it has a one-tap channel equalizer followed by a fixed mismatched filter that is sparse in the frequency domain. The system achieves both low self-interference and high spectral confinement by means of sacrificing the TF symbol density *slightly* as well as the TD localization at the RX. Moreover, it maintains low complexity by using the separate channel equalizer and fixed mismatched filter, and by optimizing the RX prototype filter under an FD sparsity constraint. Hence, among the QAM-FBMC systems with excellent spectral confinement, the system proposed in [26] shows the signal-to-interference-plus-noise ratio (SINR) performance inferior only to the QAM-FBMC systems in [18], [19], and [25] with high-complexity RXs or high overlapping factors. However, the achieved SINR performance is not yet satisfactory enough to support certain high-order modulations.

In this paper, we propose an improved QAM-FBMC system that further reduces self-interference. Like the QAM-FBMC system in [26], the proposed system relaxes the constraints on the TF symbol density *slightly* and the TD localization at the RX, and has a one-tap channel equalizer followed by a fixed mismatched RX filter. Unlike the system in [26] that employs the PHYDYAS filter at the TX and an FD sparse prototype filter at the RX, the proposed system jointly optimizes the TX and RX prototype filters without the sparsity constraint on the RX prototype filter in order to achieve further performance improvement. Consequently, the self-interference is further reduced without degrading the spectral confinement of the system because the spectral characteristics of a system are affected by the TX prototype filter, not by the RX prototype filter.

Since the RX prototype filter no longer has sparsity in the frequency domain, the proposed system uses a new polyphase network (PPN)-based structure to keep the complexity of the system low. For low complexity, PPN structures have often been used to perform the TX or RX filtering in FBMC systems [7], [8], [27]. In these systems, FD equalization is performed *after* RX filtering [6], [7], [27], which results in degradation from adjacent subcarrier interference already incurred in the RX filtering. To avoid this problem, some QAM-FBMC systems perform FD equalization *before* RX filtering without using a PPN structure at the RX [11], [12], [16], [26], and the system in [26] is one of them. The proposed system using the PPN-based structure maintains performing FD equalization *before* RX filtering to avoid the degradation. Moreover, the PPN-based structure uniquely accommodates both the excess delay and extended observation window introduced by the relaxed constraints on the TF symbol density and the TD localization at the RX. Hence, it is distinct from the ordinary PPN structures employed by other FBMC systems [8], [27], [28].

The joint optimization in this paper is formulated as an approximate SINR maximization and converted into a line search, under a constraint on the fall-off rate of the TX

prototype filter for the high spectral confinement. A lower bound on the post-processing signal-to-noise ratio (SNR) is used as the search parameter and, at each lower bound, both prototype filters are optimized to maximize the signal-to-interference ratio (SIR). Since the RX prototype filter can be written as a function of the TX prototype filter, the joint optimization problem of the TX and RX prototype filters becomes an optimization problem with the TX prototype filter as the only decision variable. Once the line search is stopped at a saturation point of the SINR, a pair of fixed TX and RX filters that achieve near-perfect bi-orthogonality is used for all SNR values.

For practical applications, we present two optimized TX prototype filters, which are suitable for slightly different use cases. Although both filters have excellent spectral confinement, the first filter is better suited for scenarios that prioritize low complexity and latency, whereas the second filter is better suited for scenarios that prioritize high spectral confinement and SIR. The performance of the systems that use the proposed PPN-based structure and these prototype filters is evaluated and compared with that of other systems. The numerical results reveal that the SINR of the proposed systems is high enough across all SNR ranges, and thus can satisfactorily support high-order modulations like 1024-QAM at high SNR regime without using a high-complexity RX, such as full-tap LMMSE or IIC, and without increasing the overlapping factor. Furthermore, the complexity of these systems is comparable to the system in [26]. In summary, the proposed systems achieve excellent spectral confinement and low complexity at the same time.

The rest of this paper is organized as follows. In Section II, the signal and system models of the proposed QAM-FBMC are presented. In Section III, the proposed PPN-based structure at the TX and RX is described. In Section IV, the joint optimization problem to find the TX and RX prototype filters is formulated, and the proposed prototype filters are presented. In Section V, the performance of the proposed systems is numerically evaluated and compared with that of other systems. Finally, in Section VI, the paper concludes with final remarks.

Throughout this paper, $\boldsymbol{A}^{\mathsf{T}}$ denotes the transpose of a matrix (or vector) $\boldsymbol{A}$, and $\boldsymbol{A}^{\mathsf{H}}$ denotes its Hermitian transpose. The notation s^* represents the complex conjugate of s. The matrices $\boldsymbol{I}_n$ and $\boldsymbol{0}_{n\times m}$ indicate the identity matrix of size n and the all-zero matrix of size $n \times m$, respectively. The diag$(\cdot)$ operator, when applied to a vector, converts it into a square matrix with its diagonal entries corresponding to the entries of the vector. When applied to a matrix, it extracts its diagonal entries into a vector. The tr$(\cdot)$ denotes the trace and $\mathbb{E}[\cdot]$ denotes the expectation. The $\odot$ operator represents the Hadamard product operator, that is, the entrywise product operator. We use a zero-based indexing system for vectors and matrices when referring to their entries, with the notable exception of the unit basis vectors. Specifically, for a vector $\boldsymbol{v}$, the notation $[\boldsymbol{v}]_n$ refers to the $(n+1)$-th entry of $\boldsymbol{v}$, where n is a non-negative integer. Similarly, for a matrix $\boldsymbol{A}$, the notation $[\boldsymbol{A}]_{m,n}$ refers to the entry at the $(m+1)$-th row and $(n+1)$-th column of $\boldsymbol{A}$, where both m and n are non-negative integers. It is important to note that the unit basis vectors begin from index 1, such as $\boldsymbol{e}_1, \boldsymbol{e}_2, \cdots$.

II. SIGNAL AND SYSTEM MODELS

In this section, we present the signal and system models for a QAM-FBMC system. The models are specifically designed for the proposed system, ensuring the system in the models can accommodate a positive excess delay or an expanded observation window. Additionally, the system has a channel equalizer, followed by a fixed mismatched filter at the RX. Note that these are also present in the system in [26], and the models are based on those of [26]. To make this paper self-contained, we briefly present some parts that are common with [26] as well as the parts that differ from the models in [26]. The signal models are described in discrete-time (DT) complex baseband.

A. TX MODEL

The QAM-FBMC signal transmitted by a TX can be written as

$$x[n] = \sum_{k=-\infty}^{\infty} \sum_{m=0}^{M-1} p_m[n - k(M+S)] d_m[k], \tag{1}$$

where M is the number of subcarriers including M_{null} null subcarriers, S is the excess delay, $p_m[n]$ as a function of n is the TX waveform for the m-th subcarrier, and $d_m[k]$ is the k-th QAM symbol at the m-th subcarrier. For any m corresponding to one of the M_{null} null subcarriers, the QAM symbol $d_m[k]$ is assigned a value of zero.

The TX waveform $p_m[n]$ for the m-th subcarrier is related to the impulse response $p_0[n]$ of the TX prototype filter, as represented by

$$p_m[n] \triangleq p_0[n] e^{\mathrm{j}2\pi \frac{mn}{M}}. \tag{2}$$

Hence, the TX waveforms for different subcarriers are essentially prototype filter responses, each individually adjusted for a specific frequency shift. The model focuses on a QAM-FBMC system that employs a single TX prototype filter for simplicity, not on a system that employs a pair of alternating prototype filters like the systems in [11], [12], and [14]. The TX waveform $p_0[n]$ is used in the following definitions of the TX TD and FD prototype vectors of length N.

Definition 1: The TX TD and FD prototype vectors are defined as

$$\boldsymbol{p}_t \triangleq \begin{bmatrix} p_0[0] & p_0[1] & \cdots & p_0[N-1] \end{bmatrix}^{\mathsf{T}} \tag{3a}$$

and

$$\boldsymbol{p}_f \triangleq \boldsymbol{W}_N \boldsymbol{p}_t, \tag{3b}$$

respectively, where $p_0[n] = 0$ for $n < 0$ or $n \geq N$, and $\boldsymbol{W}_N \in \mathbb{C}^{N\times N}$ is the unitary discrete Fourier transform (DFT) matrix of size N.

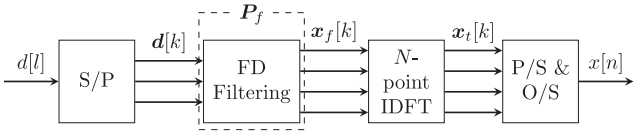

FIGURE 1. TX block diagram of QAM-FBMC system with the direct FD structure.

FIGURE 1 shows the block diagram of a QAM-FBMC TX that generates the signal $x[n]$ to transmit. The TX in FIGURE 1 is implemented by using an FD pulse-shaping filter, and this structure is referred to as the *direct FD structure* throughout this paper.

In the serial-to-parallel conversion (S/P) block of FIGURE 1, given a sequence $(d[l])_{l\in\mathbb{Z}}$ of QAM symbols, a sequence $(\boldsymbol{d}[k])_{k\in\mathbb{Z}}$ of length-M vectors is generated. The QAM symbols $d_m[k]$ in (1) and the QAM symbol vector $\boldsymbol{d}[k]$ are related as

$$\boldsymbol{d}[k] = \left[d_0[k]\ d_1[k]\ \cdots\ d_{M-1}[k]\right]^{\mathsf{T}}. \tag{4}$$

For convenience, the symbols are normalized so that

$$\mathbb{E}\left[\boldsymbol{d}[k]\boldsymbol{d}^{\mathsf{H}}[k']\right] = \delta[k-k']\tilde{\boldsymbol{I}}_M \quad \forall k, k', \tag{5}$$

where $\delta[n]$ is the unit sample function, and $\tilde{\boldsymbol{I}}_M$ is a modification of $\boldsymbol{I}_M$ in which the diagonal entries corresponding to null subcarriers are set to zero.

In the FD filtering block, the QAM symbol vector $\boldsymbol{d}[k]$ is transformed into the FD vector $\boldsymbol{x}_f[k]$. Let $\boldsymbol{C}_N \in \mathbb{R}^{N\times N}$ be the circular down-shift matrix defined by

$$\boldsymbol{C}_N \triangleq \left[\boldsymbol{e}_2\ \boldsymbol{e}_3\ \cdots\ \boldsymbol{e}_N\ \boldsymbol{e}_1\right], \tag{6}$$

and thus $\boldsymbol{C}_N^k$ circularly down-shifts a column vector of length N by k. The output $\boldsymbol{x}_f[k]$ of the block can be represented as

$$\boldsymbol{x}_f[k] = \boldsymbol{P}_f\boldsymbol{d}[k], \tag{7}$$

where $\boldsymbol{P}_f \in \mathbb{C}^{N\times M}$ is the TX FD filter matrix defined as

$$\boldsymbol{P}_f \triangleq \left[\boldsymbol{p}_f\ \boldsymbol{C}_N^K\boldsymbol{p}_f\ \cdots\ \boldsymbol{C}_N^{(M-1)K}\boldsymbol{p}_f\right] \tag{8}$$

and K is defined as

$$K \triangleq N/M. \tag{9}$$

Note that $\boldsymbol{P}_f$ is a quasi-cyclic matrix, whose $(m+1)$-th column is obtained by circular down-shifting $\boldsymbol{p}_f$ by mK. Additionally, this process is equivalent to first upsampling by K, and then applying FD pulse shaping using a circulant matrix whose first column is $\boldsymbol{p}_f$ [26]. As a result, K is referred to as the upsampling factor. Although K is often termed the overlapping factor in conventional FBMC systems with $S = 0$, this terminology is not suitable for K when $S > 0$. Instead, a different quantity serves as the overlapping factor, which will be further discussed later in this subsection.

In the inverse discrete Fourier transform (IDFT) block, the FD vector $\boldsymbol{x}_f[k]$ is converted into the FBMC symbol vector $\boldsymbol{x}_t[k]$ as

$$\boldsymbol{x}_t[k] = \boldsymbol{W}_N^{\mathsf{H}}\boldsymbol{x}_f[k] = \boldsymbol{W}_N^{\mathsf{H}}\boldsymbol{P}_f\boldsymbol{d}[k]. \tag{10}$$

The fast Fourier transform (FFT) algorithm can be used to implement this block efficiently, particularly when N is a power of two.

In the parallel-to-serial conversion (P/S) and overlap-and-sum (O/S) block, a sequence $(\boldsymbol{x}_t[k])_k$ of FBMC symbol vectors is converted to a DT signal $(x[n])_n$ through P/S and O/S operations. The output $(x[n])_n$ is the O/S of the FBMC symbol vectors given by

$$x[n] = \sum_{k=-\infty}^{\infty} [\boldsymbol{x}_t[k]]_{n-k(M+S)}, \tag{11}$$

where $[\boldsymbol{x}_t[k]]_n$ for $n = 0, 1, \cdots, N-1$ is the $(n+1)$-th entry of $\boldsymbol{x}_t[k]$ of length N, and $[\boldsymbol{x}_t[k]]_n = 0$ for $n < 0$ or $n \geq N$. Hence, the k-th FBMC symbol is parallel-to-serial converted and delayed by $k(M+S)$. If N exceeds $M+S$, which results in pulse overlaps between adjacent FBMC symbols, the overlapping symbols are consequently superimposed and summed in the time domain. The overlapping factor, representing the average number of overlapped FBMC symbols contributing to $x[n]$, is denoted as

$$K_{\text{avg}} \triangleq \frac{N}{M+S}, \tag{12}$$

from which it follows that $K_{\text{avg}} = K$ if $S = 0$ and $K_{\text{avg}} < K$ if $S > 0$.

To briefly compare the data transmission efficiencies of different systems, we define the *TF-product* as the product of the symbol period and the subcarrier spacing [6], [26], which is represented by

$$TF \triangleq \frac{M+S}{M} \tag{13}$$

in terms of the parameters we have previously defined. This is equivalent to the reciprocal of the TF symbol density. In CP-OFDM systems, M and S correspond to the size of the IDFT matrix and the length of the CP, respectively. For instance, the CP-OFDM system described in [1] has a TF value of approximately 1.07, whereas the conventional QAM-FBMC systems detailed in [11], [12], [14], [16], [18], [29], [30], and [19] have a TF value of 1. The proposed QAM-FBMC system in this paper has a TF-product slightly greater than unity, similar to the system in [26]. Specifically, the TF value of the proposed system is 1.0625 with an excess delay $S = M/16$.

B. CHANNEL AND RX MODELS

The channel is assumed to be slowly time-varying and subjected to additive noise. During the transmission of the

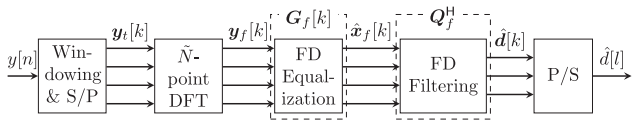

FIGURE 2. RX block diagram of QAM-FBMC system with the direct FD structure.

k-th QAM symbol vector $\boldsymbol{d}[k]$, the complex envelope of the DT received signal, $y[n]$, is represented by

$$y[n] = \sum_{m=0}^{L_{\text{ch}}-1} h^{(k)}[m]x[n-m] + w[n], \tag{14}$$

where $h^{(k)}[n]$ is the impulse response of the channel for the k-th FBMC symbol, L_{ch} is the channel length, and $w[n]$ is the additive white Gaussian noise (AWGN). The channel is approximated by a linear time-invariant (LTI) system for each symbol transmission.

FIGURE 2 shows the block diagram of the QAM-FBMC RX that takes $y[n]$ as input and produces the estimated QAM symbol $\hat{d}[l]$ as output. The RX employs an FD filter, which is either matched or mismatched to the TX filter. This structure is also termed the direct FD structure, consistent with the terminology used for the TX.

In the windowing and S/P block of FIGURE 2, the received signal $(y[n])_n$ is windowed and converted into a sequence $(\boldsymbol{y}_t[k])_k$ of vectors of length $\tilde{N}$, where $\tilde{N}$ is the length of the observation window. In conventional QAM-FBMC systems [11], [12], [14], [16], [18], [19], [29], [30], the length $\tilde{N}$ is equal to N. However, it can be extended both forward and backward from the conventional length-N window by L_{pre} and L_{post}, respectively, in order to improve the RX performance [26]. Thus, in the proposed system, $\tilde{N}$ is defined as

$$\tilde{N} \triangleq L_{\text{pre}} + N + L_{\text{post}}. \tag{15}$$

Also, we define r and $\tilde{K}$ as

$$r \triangleq \frac{\tilde{N}}{N} \quad \text{and} \quad \tilde{K} \triangleq rK. \tag{16}$$

In the following discussions, we set L_{pre} equal to L_{post}. Thus, $L_{\text{add}} \triangleq L_{\text{pre}} = L_{\text{post}}$. The output $\boldsymbol{y}_t[k] \in \mathbb{C}^{\tilde{N}\times 1}$ of the block, which we refer to as a windowed signal vector, is then given by

$$\boldsymbol{y}_t[k] \triangleq \begin{bmatrix} y[k(M+S)-L_{\text{add}}] \\ y[k(M+S)-L_{\text{add}}+1] \\ \vdots \\ y[k(M+S)+N+L_{\text{add}}-1] \end{bmatrix} \tag{17}$$

in terms of $y[n]$.

To express $\boldsymbol{y}_t[k]$ in terms of the transmitted signal $x[n]$, we first define the TD channel matrix $\boldsymbol{H}_t[k]$ and the signal vector $\tilde{\boldsymbol{x}}_t[k]$. The TD channel matrix $\boldsymbol{H}_t[k] \in \mathbb{C}^{(\tilde{N}+L_{\text{ch}}-1)\times(\tilde{N}+L_{\text{ch}}-1)}$ is a Toeplitz matrix with its first column given by $\left[h^{(k)}[0]\ h^{(k)}[1]\ \cdots\ h^{(k)}[\tilde{N}+L_{\text{ch}}-2]\right]^{\mathsf{T}}$. The signal vector $\tilde{\boldsymbol{x}}_t[k] \in \mathbb{C}^{(\tilde{N}+L_{\text{ch}}-1)\times 1}$ is defined by

$$\tilde{\boldsymbol{x}}_t[k] = \begin{bmatrix} x[k(M+S)-L_{\text{add}}-L_{\text{ch}}+1] \\ x[k(M+S)-L_{\text{add}}-L_{\text{ch}}+2] \\ \vdots \\ x[k(M+S)+N+L_{\text{add}}-1] \end{bmatrix}, \tag{18}$$

which is a vector of the transmitted signal $x[n]$. Consequently, the windowed signal vector $\boldsymbol{y}_t[k]$ can be expressed as

$$\boldsymbol{y}_t[k] = \boldsymbol{T}\boldsymbol{H}_t[k]\tilde{\boldsymbol{x}}_t[k] + \boldsymbol{w}[k], \tag{19}$$

where the row-pruning matrix $\boldsymbol{T} \in \mathbb{C}^{\tilde{N}\times(\tilde{N}+L_{\text{ch}}-1)}$ is defined by

$$\boldsymbol{T} = \left[\boldsymbol{0}_{\tilde{N}\times(L_{\text{ch}}-1)}\ \boldsymbol{I}_{\tilde{N}}\right] \tag{20}$$

which prunes the top $(L_{\text{ch}}-1)$ rows of $\boldsymbol{H}_t[k]\tilde{\boldsymbol{x}}_t[k]$. The vector $\boldsymbol{w}[k] \sim \mathcal{CN}(\boldsymbol{0}_{\tilde{N}\times 1}, \sigma_W^2\boldsymbol{I}_{\tilde{N}})$ is a proper-complex AWGN vector with variance σ_W^2.

In the DFT block, the windowed signal vector $\boldsymbol{y}_t[k]$ is converted into the FD vector $\boldsymbol{y}_f[k]$ as

$$\boldsymbol{y}_f[k] = \boldsymbol{W}_{\tilde{N}}\boldsymbol{y}_t[k], \tag{21}$$

where the FFT algorithm can be used for efficiency, particularly when $\tilde{N}$ is a power of two.

In the FD equalization block, the channel effect on $\boldsymbol{y}_f[k]$ is mitigated to generate the output $\hat{\boldsymbol{x}}_f[k]$. The output $\hat{\boldsymbol{x}}_f[k]$ is given by

$$\hat{\boldsymbol{x}}_f[k] = \boldsymbol{G}_f[k]\boldsymbol{y}_f[k], \tag{22}$$

where $\boldsymbol{G}_f[k]$ is the time-varying channel equalization matrix for the k-th FBMC symbol vector. This matrix $\boldsymbol{G}_f[k]$ is optimized so that its output $\boldsymbol{G}_f[k]\boldsymbol{y}_f[k]$ can approximate $\boldsymbol{W}_{\tilde{N}}\boldsymbol{T}\tilde{\boldsymbol{x}}_t[k]$ as closely as possible, thereby mitigating the channel effect [26]. The optimization problem to find the optimal $\boldsymbol{G}_f[k]$ is expressed as

$$\underset{\boldsymbol{G}_f[k]}{\text{minimize}}\ \mathbb{E}\left[\left\|\boldsymbol{G}_f[k]\boldsymbol{y}_f[k] - \boldsymbol{W}_{\tilde{N}}\boldsymbol{T}\tilde{\boldsymbol{x}}_t[k]\right\|^2\right]. \tag{23}$$

The solution to this problem can yield the full-tap LMMSE equalization matrix $\boldsymbol{G}_f[k]$ [26]. However, determining the exact solution every time the channel matrix $\boldsymbol{H}_t[k]$ changes can be computationally intensive.

In order to reduce the complexity of the RX, we use the one-tap LMMSE equalization matrix $\boldsymbol{G}_{f,\text{one}}[k]$ as an approximation for $\boldsymbol{G}_f[k]$, based on the approach described in [26]. Let us define $\tilde{\boldsymbol{H}}_f$ as the diagonalized FD channel matrix represented by

$$\tilde{\boldsymbol{H}}_f[k] \triangleq \text{diag}(\text{diag}(\boldsymbol{W}_{\tilde{N}}\boldsymbol{T}\hat{\boldsymbol{H}}_t[k]\boldsymbol{T}^{\mathsf{T}}\boldsymbol{W}_{\tilde{N}}^{\mathsf{H}})). \tag{24}$$

We also define $\tilde{\boldsymbol{R}}_f$ as the correlation matrix of $\boldsymbol{W}_{\tilde{N}}\boldsymbol{T}\tilde{\boldsymbol{x}}_t[k]$. Then, the one-tap LMMSE equalization matrix $\boldsymbol{G}_{f,\text{one}}[k]$ is given by

$$\boldsymbol{G}_{f,\text{one}}[k] \triangleq \tilde{\boldsymbol{H}}_f^{\mathsf{H}}[k]\left(\tilde{\boldsymbol{H}}_f[k]\tilde{\boldsymbol{H}}_f^{\mathsf{H}}[k] + \frac{\sigma_W^2}{\sigma_S^2}\boldsymbol{I}_{\tilde{N}}\right)^{-1}, \tag{25}$$

where σ_S^2 is the signal variance, which is the mean of the diagonal entries of $\tilde{\boldsymbol{R}}_f$ with null subcarriers excluded.

In the FD filtering block, the output $\hat{\boldsymbol{x}}_f[k]$ from the equalizer is processed to obtain the estimate $\hat{\boldsymbol{d}}[k]$ of the QAM symbol vector $\boldsymbol{d}[k]$. This estimate $\hat{\boldsymbol{d}}[k]$ can be expressed as

$$\hat{\boldsymbol{d}}[k] = \boldsymbol{Q}_f^{\mathsf{H}} \hat{\boldsymbol{x}}_f[k], \tag{26}$$

where $\boldsymbol{Q}_f^{\mathsf{H}}$ is the RX FD filter matrix. In QAM-FBMC systems, like those in [12] and [16], which employ a matched RX filter and have $\tilde{N} = N$, the RX FD filter matrix is equal to the Hermitian conjugate of the TX FD filter matrix, i.e., $\boldsymbol{Q}_f^{\mathsf{H}} = \boldsymbol{P}_f^{\mathsf{H}}$. However, in the proposed system which employs a mismatched filter and has $\tilde{N} > N$, the RX FD filter matrix $\boldsymbol{Q}_f^{\mathsf{H}}$ differs from $\boldsymbol{P}_f^{\mathsf{H}}$.

In the proposed system, the mismatched filter is constructed using an RX prototype filter, analogous to the construction of the TX FD filter that uses a TX prototype filter. This enables the RX to use the PPN-based structure, and also simplifies the joint optimization process of the filters. The details of the PPN-based structure and the optimization will be discussed in the following sections.

Analogous to (2) for the TX, the impulse response $q_0[n]$ of the RX prototype filter is related to the waveform $q_m[n]$ for the m-th subcarrier, as represented by

$$q_m[n] \triangleq q_0[n] e^{\mathrm{j}2\pi \frac{mn}{M}}. \tag{27}$$

In other words, the RX waveforms for different subcarriers are essentially RX prototype filter responses, each individually adjusted for a specific frequency shift. To proceed further, we define the RX TD and FD prototype vectors.

Definition 2: The RX TD and FD prototype vectors are defined as

$$\boldsymbol{q}_t \triangleq [q_0[-L_{\mathrm{add}}] \quad q_0[-L_{\mathrm{add}}+1] \quad \cdots \quad q_0[N+L_{\mathrm{add}}-1]]^{\mathsf{T}} \tag{28a}$$

and

$$\boldsymbol{q}_f \triangleq \boldsymbol{W}_{\tilde{N}} \boldsymbol{q}_t, \tag{28b}$$

respectively, where $q_0[n] = 0$ for $n < -L_{\mathrm{add}}$ or $n \geq N + L_{\mathrm{add}}$.

The RX FD prototype vector $\boldsymbol{q}_f$ corresponds to the first column of $\boldsymbol{Q}_f$. Subsequently, it is shown that the matrix $\boldsymbol{Q}_f$ can be expressed in terms of the vector $\boldsymbol{q}_f$. To begin, let us define $\tilde{\boldsymbol{C}}$ as

$$\tilde{\boldsymbol{C}} = (-1)^{m(\tilde{K}-K)} \boldsymbol{C}_{\tilde{N}}^{\tilde{K}}, \tag{29}$$

where $\boldsymbol{C}_{\tilde{N}}$ is the circular down-shift matrix of size $\tilde{N}$.

Proposition 1: The Hermitian conjugate $\boldsymbol{Q}_f$ of the RX FD filter matrix can be written as

$$\boldsymbol{Q}_f = \left[\tilde{\boldsymbol{C}}^0 \boldsymbol{q}_f \;\; \tilde{\boldsymbol{C}}^1 \boldsymbol{q}_f \;\; \cdots \;\; \tilde{\boldsymbol{C}}^{M-1} \boldsymbol{q}_f \right]. \tag{30}$$

Proof: For $n = 0, 1, \ldots, \tilde{N}-1$, the $(n+1)$-th component of $\boldsymbol{q}_f$, which is the first column of $\boldsymbol{Q}_f$, is given by

$$[\boldsymbol{q}_f]_n = \sum_{l=0}^{\tilde{N}-1} q_0[l - L_{\mathrm{add}}] e^{-\mathrm{j}2\pi \frac{ln}{\tilde{N}}}. \tag{31}$$

Then, for $n = 0, 1, \ldots, \tilde{N}-1$, the $(n+1)$-th component of the $(m+1)$-th column of $\boldsymbol{Q}_f$ is expressed as

$$[\boldsymbol{Q}_f]_{n,m} = \sum_{l=0}^{\tilde{N}-1} \left(q_0[l - L_{\mathrm{add}}] e^{\mathrm{j}2\pi \frac{m(l-L_{\mathrm{add}})}{M}} \right) e^{-\mathrm{j}2\pi \frac{ln}{\tilde{N}}} \tag{32a}$$

$$= \sum_{l=0}^{\tilde{N}-1} q_0[l - L_{\mathrm{add}}] e^{\mathrm{j}2\pi \frac{m(l-L_{\mathrm{add}})\tilde{K}}{\tilde{N}}} e^{-\mathrm{j}2\pi \frac{ln}{\tilde{N}}} \tag{32b}$$

$$= \sum_{l=0}^{\tilde{N}-1} q_0[l - L_{\mathrm{add}}] e^{-\mathrm{j}2\pi \frac{l(n-m\tilde{K})}{\tilde{N}}} e^{-\mathrm{j}2\pi \frac{L_{\mathrm{add}} m\tilde{K}}{\tilde{N}}} \tag{32c}$$

$$= e^{-\mathrm{j}2\pi \frac{L_{\mathrm{add}} m}{M}} [\boldsymbol{q}_f]_{\mathrm{mod}\left(n-m\tilde{K},\tilde{N}\right)}, \tag{32d}$$

where we have used the relation $\tilde{N}/\tilde{K} = M$ and (27). From the relation $\tilde{N} = N + 2L_{\mathrm{add}}$, we have

$$[\boldsymbol{Q}_f]_{n,m} = e^{-\mathrm{j}2\pi \frac{(\tilde{N}-N)m}{2M}} [\boldsymbol{q}_f]_{\mathrm{mod}\left(n-m\tilde{K},\tilde{N}\right)} \tag{32e}$$

$$= (-1)^{m(\tilde{K}-K)} [\boldsymbol{q}_f]_{\mathrm{mod}\left(n-m\tilde{K},\tilde{N}\right)}, \tag{32f}$$

where we have used the relations $\tilde{N}/M = \tilde{K}$ and $N/M = K$. Hence, the $(m+1)$-th column of $\boldsymbol{Q}_f$ is determined by applying a downward circular shift of $m\tilde{K}$ components to its first column $\boldsymbol{q}_f$ and then multiplying by $(-1)^{m(\tilde{K}-K)}$. □

When both K and r are even integers, each column of $\boldsymbol{Q}_f$ is a downward circular shift of the first column without any phase factor and $\boldsymbol{Q}_f$ becomes a quasi-cyclic matrix. Hence, the system proposed in [26] with $K = 4$ and $r = 2$ stands as a special case of this model.

Lastly, in the P/S block, the sequence $(\hat{\boldsymbol{d}}[k])_k$ of estimates of the QAM symbol vectors is converted into a sequence $(\hat{d}[l])_l$ of estimates of the QAM symbols.

Contrary to the RX presented here, it is worth mentioning that the LMMSE RX can be employed, similar to the system described in [18]. This type of RX effectively combines the functionalities of the channel equalizer and symbol detector and attempts to solve the optimization problem given by

$$\underset{\boldsymbol{L}[k]}{\text{minimize}}\, \mathbb{E}\left[\|\boldsymbol{L}[k]\boldsymbol{y}_t[k] - \boldsymbol{d}[k]\|^2 \right]. \tag{33a}$$

However, this type of RX inherently carries significant computational complexity. The LMMSE matrix $\boldsymbol{L}[k]$ depends on the slowly varying channel $\boldsymbol{H}_t[k]$, and updating the solution to the LMMSE problem each time the channel changes can be computationally demanding [26]. As a combination of a channel equalizer and a symbol detector, the LMMSE RX may require even more complex computations than the full-tap LMMSE equalizer that can be derived from (23).

III. PPN-BASED STRUCTURE

In this section, we present the proposed PPN-based structure at the TX and RX. Given that a positive excess delay $S > 0$ and an extended observation window $\tilde{N} > N$ are integrated into the proposed system, a direct adaptation of the PPN

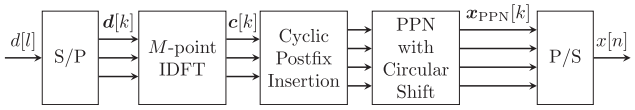

FIGURE 3. TX block diagram of QAM-FBMC system with the PPN-based structure.

structure of the conventional FBMC systems is infeasible. Hence, we develop a new structure based on the PPN structure found in other FBMC systems [27].

A. TX

The new structure for the TX of the proposed system is based on the conventional PPN as illustrated in its block diagram in FIGURE 3, Compared to the direct FD structure described in the previous section, this new structure typically offers a substantial reduction in computational complexity. It is similar to the polyphase synthesis filter bank to transform the QAM symbol vectors into the FBMC signal in other FBMC systems [27].

A structure based on the PPN with $(M + S)$ polyphase subfilters is utilized for the generation of the FBMC signal $x[n]$. The QAM symbol vector $\boldsymbol{d}[k]$ is first transformed into the vector $\boldsymbol{c}[k] = \left[c_0[k]\ c_1[k]\ \cdots\ c_{M-1}[k]\right]^{\mathsf{T}}$ using the IDFT as

$$\boldsymbol{c}[k] \triangleq \sqrt{M}\boldsymbol{W}_M^{\mathsf{H}}\boldsymbol{d}[k], \tag{34}$$

where $\boldsymbol{W}_M$ is the unitary DFT matrix of size M.

The output $\boldsymbol{c}[k]$ is then transformed into $\tilde{\boldsymbol{c}}[k,l] = \left[\tilde{c}_0[k]\ \tilde{c}_1[k]\ \cdots\ \tilde{c}_{M+S-1}[k]\right]^{\mathsf{T}}$, where each component is given by

$$\tilde{c}_n[k,l] = c_{\mathrm{mod}(n+lS,M)}[k] \tag{35}$$

for $n = 0, 1, \cdots, M + S - 1$. This transformation can be implemented by adding a cyclic postfix of length S and performing a circular shift for each $l = 0, 1, \cdots, K-1$. The transformed vector $\tilde{\boldsymbol{c}}[k,l]$ is then component-wise multiplied and summed to generate the FBMC signal vector for the k-th QAM symbol vector. The vectors $\boldsymbol{x}_{\mathrm{PPN}}[k]$ and $\boldsymbol{p}_{\mathrm{PPN}}[l]$, both belonging to $\mathbb{C}^{(M+S)\times 1}$, are defined as

$$\boldsymbol{x}_{\mathrm{PPN}}[k] \triangleq \begin{bmatrix} x[k(M+S)] \\ x[k(M+S)+1] \\ \vdots \\ x[k(M+S)+(M+S-1)] \end{bmatrix} \tag{36a}$$

and

$$\boldsymbol{p}_{\mathrm{PPN}}[l] \triangleq \begin{bmatrix} p_0[l(M+S)] \\ p_0[l(M+S)+1] \\ \vdots \\ p_0[l(M+S)+(M+S-1)] \end{bmatrix}, \tag{36b}$$

respectively. Then, $\boldsymbol{x}_{\mathrm{PPN}}[k]$ can be expressed as

$$\boldsymbol{x}_{\mathrm{PPN}}[k] = \sum_{l=0}^{K-1} \boldsymbol{p}_{\mathrm{PPN}}[l] \odot \tilde{\boldsymbol{c}}[k-l,l]. \tag{36c}$$

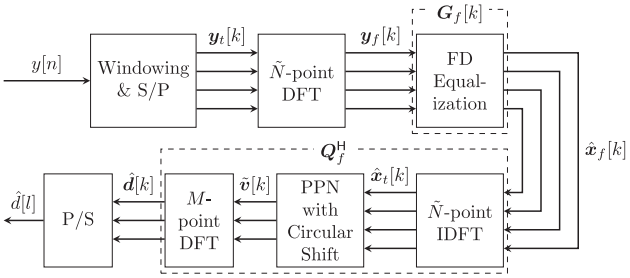

FIGURE 4. RX block diagram of QAM-FBMC system with the PPN-based structure.

This output is then converted by the P/S into the DT signal $x[n]$. The generated FBMC signal $x[n]$ is equivalent to the signal in (1) and (11). This structure can be used in systems even with an excess delay $S > 0$.

We show that the PPN-based structure indeed produces the signal in (1) as follows.

Proposition 2: The output $x[n]$ of the TX using the PPN-based structure as presented in (36a) and (36c) is equal to the signal to transmit by the TX as defined in (1).

Proof: From (1) and (2), $x[k(M+S)+n]$ is given by

$$x[k(M+S)+n] = \sum_{l=-\infty}^{\infty}\sum_{m=0}^{M-1} p_m[(k-l)(M+S)+n]d_m[l] \tag{37}$$

On the other hand, for $n = 0, 1, \cdots, M+S-1$, the $(n+1)$-th component of $\boldsymbol{x}_{\mathrm{PPN}}[k]$ in (36c) is given by

$$\begin{aligned}
&[\boldsymbol{x}_{\mathrm{PPN}}[k]]_n \\
&= \sum_{l=0}^{K-1} p_0[l(M+S)+n]\tilde{c}_n[k-l,l] && \text{(38a)}\\
&= \sum_{l=0}^{K-1} p_0[l(M+S)+n]\sum_{m=0}^{M-1} d_m[k-l]e^{\mathrm{j}2\pi\frac{m(n+lS)}{M}} && \text{(38b)}\\
&= \sum_{l=-\infty}^{\infty} p_0[(k-l)(M+S)+n]\sum_{m=0}^{M-1} d_m[l]e^{\mathrm{j}2\pi\frac{m((k-l)S+n)}{M}} && \text{(38c)}\\
&= \sum_{l=-\infty}^{\infty} p_m[(k-l)(M+S)+n]\sum_{m=0}^{M-1} d_m[l] && \text{(38d)}\\
&= x[k(M+S)+n], && \text{(38e)}
\end{aligned}$$

which completes the proof. □

Note that this PPN-based structure is similar to one of the TX PPN structures provided in [28]. However, rather than pre-multiplying phase shifts prior to the IDFT, we circularly shift the intermediate vector.

B. RX

The RX FD filter $\boldsymbol{Q}_f^{\mathsf{H}}$ can be constructed by using a new structure based on the PPN. The entire RX using this

PPN-based RX FD filter is illustrated in the block diagram in FIGURE 4. In particular, a structure based on the polyphase analysis filter bank is employed to derive the estimated QAM symbol vector $\hat{\boldsymbol{d}}[k]$ from the equalizer output vector $\hat{\boldsymbol{x}}_f[k]$. This can reduce the computational complexity of the RX FD filter, especially when the number of nonzero FD coefficients of the RX prototype vector $\boldsymbol{q}_f$ is large.

The equalizer output vector $\hat{\boldsymbol{x}}_f[k]$ is first transformed back to the time domain by the IDFT operation, given by

$$\hat{\boldsymbol{x}}_t[k] = \boldsymbol{W}_{\tilde{N}}^{\mathsf{H}} \hat{\boldsymbol{x}}_f[k], \tag{39}$$

This transformation is necessary because the input of the polyphase analysis filter bank should be in the time domain.

We begin by defining K_u and K_w as

$$K_u = \left\lceil * \frac{L_{\text{add}}}{M+S} \right\rceil \text{ and } K_w = \left\lceil * \frac{KM + L_{\text{add}}}{M+S} \right\rceil - 1. \tag{40}$$

Next, we introduce the vectors $\hat{\boldsymbol{x}}_{t,\text{PPN},i}[k]$ and $\boldsymbol{q}_{\text{PPN},i}[l]$ for $i = 0, 1$, all of which belong to $\mathbb{C}^{M\times 1}$. These vectors are defined as

$$\hat{\boldsymbol{x}}_{t,\text{PPN},0}[k] \triangleq \begin{bmatrix} [\hat{\boldsymbol{x}}_t[k]]_{L_{\text{add}}+l(M+S)} \\ \vdots \\ [\hat{\boldsymbol{x}}_t[k]]_{L_{\text{add}}+l(M+S)+(M-1)} \end{bmatrix}$$

$$\hat{\boldsymbol{x}}_{t,\text{PPN},1}[k] \triangleq \begin{bmatrix} [\hat{\boldsymbol{x}}_t[k]]_{L_{\text{add}}+l(M+S)+M} \\ \vdots \\ [\hat{\boldsymbol{x}}_t[k]]_{L_{\text{add}}+l(M+S)+(M+S-1)} \\ \boldsymbol{0}_{(M-S)\times 1} \end{bmatrix} \tag{41a}$$

and

$$\boldsymbol{q}_{\text{PPN},0}[l] \triangleq \begin{bmatrix} q_0[l(M+S)] \\ q_0[l(M+S)+1] \\ \vdots \\ q_0[l(M+S)+(M-1)] \end{bmatrix}$$

$$\boldsymbol{q}_{\text{PPN},1}[l] \triangleq \begin{bmatrix} q_0[l(M+S)+M] \\ \vdots \\ q_0[l(M+S)+(M+S-1)] \\ \boldsymbol{0}_{(M-S)\times 1} \end{bmatrix} \tag{41b}$$

respectively. Subsequently, the output $\hat{\boldsymbol{x}}_t[k]$ of the IDFT operation is processed through a component that is based on M polyphase subfilters, resulting in the vector $\boldsymbol{v}[k,l]$. This operation can be represented as

$$\boldsymbol{v}[k,l] = \boldsymbol{q}^*_{\text{PPN},0}[l] \odot \hat{\boldsymbol{x}}_{t,\text{PPN},0}[k] + \boldsymbol{q}^*_{\text{PPN},1}[l] \odot \hat{\boldsymbol{x}}_{t,\text{PPN},1}[k] \tag{41c}$$

for $l = -K_u, -K_u+1, \cdots, K_w$. Any components of $\hat{\boldsymbol{x}}_t[k]$ with indices less than 0 or larger than $\tilde{N}-1$ are considered to be 0.

We define $\tilde{\boldsymbol{v}}[k]$ whose $(n+1)$-th component $\tilde{v}_n[k]$ is given by

$$\tilde{v}_n[k] = \sum_{l=-K_u}^{K_w} v_{\text{mod}(n-lS,M)}[k,l] \tag{42}$$

for $n = 0, 1, \cdots, M$. The vector $\tilde{\boldsymbol{v}}[k]$ is then transformed into the vector $\hat{\boldsymbol{d}}[k]$ by applying the DFT, which is given by

$$\hat{\boldsymbol{d}}[k] = \sqrt{M}\boldsymbol{W}_M \tilde{\boldsymbol{v}}[k]. \tag{43}$$

This structure can be used in systems even with an excess delay $S > 0$ and an extended observation window $\tilde{N} > N$.

We show that the RX FD filter implemented with the PPN-based structure is equivalent to that with the direct FD structure.

Proposition 3: The output from the RX FD filter, as presented in (43), which uses the PPN-based structure, corresponds to the estimated QAM symbol vector $\hat{\boldsymbol{d}}[k]$ in (26).

Proof: The $(m+1)$-th component of the right-hand side of (43) is given by

$$[\sqrt{M}\boldsymbol{W}_M \tilde{\boldsymbol{v}}[k]]_m$$

$$= \sum_{n=0}^{M-1} e^{-\text{j}2\pi \frac{mn}{M}} \sum_{l=-K_u}^{K_w} v_{\text{mod}(n-lS,M)}[k,l] \tag{44a}$$

$$= \sum_{n=0}^{M-1} \sum_{l=-K_u}^{K_w} v_n[k,l] e^{-\text{j}2\pi \frac{m(n+lS)}{M}} \tag{44b}$$

$$= \sum_{n=0}^{M+S-1} e^{-\text{j}2\pi \frac{mn}{M}} \sum_{l=-K_u}^{K_w} q_0^*[l(M+S)+n] \, [\hat{\boldsymbol{x}}_t[k]]_{L_{\text{add}}+l(M+S)+n} e^{-\text{j}2\pi \frac{mlS}{M}} \tag{44c}$$

$$= \sum_{l=-K_u}^{K_w} \sum_{n=0}^{M+S-1} q_0^*[l(M+S)+n] \, [\hat{\boldsymbol{x}}_t[k]]_{L_{\text{add}}+l(M+S)+n} e^{-\text{j}2\pi \frac{m(l(M+S)+n)}{M}} \tag{44d}$$

$$= \sum_{n=-L_{\text{add}}}^{KM+L_{\text{add}}-1} q_0^*[n] [\hat{\boldsymbol{x}}_t[k]]_{L_{\text{add}}+n} e^{-\text{j}2\pi \frac{mn}{M}} \tag{44e}$$

$$= \sum_{n=-L_{\text{add}}}^{KM+L_{\text{add}}-1} q_m^*[n] [\hat{\boldsymbol{x}}_t[k]]_{L_{\text{add}}+n}, \tag{44f}$$

which is equal to $(\boldsymbol{Q}_f \boldsymbol{e}_{m+1})^{\mathsf{H}} \hat{\boldsymbol{x}}_f[k] = [\boldsymbol{Q}_f^{\mathsf{H}} \hat{\boldsymbol{x}}_f[k]]_m$ in the frequency domain. □

In FIGURE 4, as opposed to the proposed system structure, one could consider moving the entire RX FD filter to a position ahead of the FD equalizer, rather than positioning it behind. This would make the $\tilde{N}$-point DFT and IDFT operations cancel out. Such an arrangement has the potential to reduce the overall complexity of the RX, as it would perform fewer DFT and IDFT operations and would allow equalization on a vector of length M instead of a large $\tilde{N}$. This structure would be similar to the conventional OQAM-FBMC structure where equalization is the concluding process. However, it is worth noting that such an arrangement might lead to decreased RX performance, especially in situations where the channel is highly frequency-selective, as highlighted in [12]

and Section V. This performance degradation occurs because the RX FD filter would be applied to a signal heavily affected by the channel, rather than to a signal where interference has been mitigated.

IV. JOINT FILTER OPTIMIZATION

In this section, we describe our method for the joint optimization of the TX and RX prototype filters. The optimization is formulated as an approximate SINR maximization, which is the SIR maximization subject to a constraint on the post-processing SNR lower bound. Since maximizing the SIR is equivalent to minimizing the mean squared error (MSE) ignoring the noise [31], the prototype filters are optimized such that the MSE in the noiseless AWGN channel is minimized. It is shown that the RX prototype filter that maximizes the SIR is a function of the TX prototype filter, and our joint optimization is simplified to an optimization with the TX prototype filter as the only decision variable. Under a constraint on the fall-off rate for high spectral confinement, the approximate SINR maximization is converted to a line search with the SNR lower bound as the search parameter. At each search-parameter value, the filters are optimized to maximize the SIR. We conclude this section by presenting the coefficients of the proposed prototype filters.

A. OBJECTIVE FUNCTION

For the proposed system to achieve high SINR performance, the TX and RX prototype filters are jointly optimized. The SINR maximization can be approximated by maximizing the SIR given a lower bound on the post-processing SNR, which can be represented by

$$\min_{\boldsymbol{p}_f,\boldsymbol{q}_f} \frac{1}{\mathrm{SINR}} = \min_{\boldsymbol{p}_f,\boldsymbol{q}_f}\left(\frac{1}{\mathrm{SIR}}+\frac{1}{\mathrm{SNR}}\right) \le \min_{\boldsymbol{p}_f,\boldsymbol{q}_f} \frac{1}{\mathrm{SIR}}+\frac{1}{\Omega_{\mathrm{SNR}}}, \tag{45}$$

where Ω_{SNR} is a lower bound on the post-processing SNR, i.e., $\mathrm{SNR} \ge \Omega_{\mathrm{SNR}}$. Hence, in this subsection, we present the objective function of the joint optimization problem, which is shown to be the SIR maximization in essence. Then, the approximate SINR maximization can be converted to a line search to maximize the SIR using the SNR lower bound as the search parameter, which is further investigated in a later subsection.

We start by deriving the SIR maximization from the optimization of the mismatched RX filter as follows. Since the input of the mismatched RX filter is the output of the FD equalizer, the channel effect of the input of the filter is designed to be minimized [26]. Hence, the mismatched RX filter is designed to minimize the MSE between the transmitted QAM symbol vector $\boldsymbol{d}[k]$ and its estimated counterpart $\hat{\boldsymbol{d}}[k]$ in an AWGN channel.

We first express the input of the mismatched filter assuming the channel effect is fully mitigated. Let us define a time-shift matrix $\boldsymbol{E}[i]$, which is of size $\tilde{N} \times N$, given by

$$\boldsymbol{E}[i] \triangleq \begin{cases} \begin{bmatrix} \boldsymbol{0}_{r_{1,i}\times c_{1,i}} & \boldsymbol{I}_{r_{1,i}} \\ \boldsymbol{0}_{(L_{\mathrm{add}}-i(M+S))\times N} \end{bmatrix}, & \text{for } i \le -\dfrac{L_{\mathrm{add}}}{M+S} \\ \begin{bmatrix} \boldsymbol{0}_{(L_{\mathrm{add}}+i(M+S))\times N} \\ \boldsymbol{I}_{r_{2,i}} \ \boldsymbol{0}_{r_{2,i}\times c_{2,i}} \end{bmatrix}, & \text{for } i > \dfrac{L_{\mathrm{add}}}{M+S} \\ \begin{bmatrix} \boldsymbol{0}_{(L_{\mathrm{add}}+i(M+S))\times N} \\ \boldsymbol{I}_N \\ \boldsymbol{0}_{(L_{\mathrm{add}}-i(M+S))\times N} \end{bmatrix}, & \text{elsewhere,} \end{cases} \tag{46a}$$

where the numbers of rows or columns $r_{1,i}$, $c_{1,i}$, $r_{2,i}$, and $c_{2,i}$ are given by

$$r_{1,i} \triangleq N + L_{\mathrm{add}} + i(M+S), \tag{46b}$$
$$c_{1,i} \triangleq -L_{\mathrm{add}} - i(M+S), \tag{46c}$$
$$r_{2,i} \triangleq N + L_{\mathrm{add}} - i(M+S), \text{ and} \tag{46d}$$
$$c_{2,i} \triangleq -L_{\mathrm{add}} + i(M+S), \tag{46e}$$

respectively. Let $\tilde{\boldsymbol{P}}_f[i] \in \mathbb{C}^{\tilde{N}\times M}$ be the time-shifted TX FD filter matrix given by

$$\tilde{\boldsymbol{P}}_f[i] \triangleq \boldsymbol{W}_{\tilde{N}}\boldsymbol{E}[i]\boldsymbol{W}_N^{\mathsf{H}}\boldsymbol{P}_f. \tag{47}$$

Then, in the noiseless AWGN channel, the output of the mismatched filter for the k-th QAM symbol vector is given by

$$\hat{\boldsymbol{d}}_{\mathrm{opt}}[k] = \sum_{i=-K_w}^{K_w} \boldsymbol{Q}_f^{\mathsf{H}}\tilde{\boldsymbol{P}}_f[i]\boldsymbol{d}[k+i]. \tag{48}$$

The optimization problem for the mismatched filter can be formulated to minimize the MSE between $\hat{\boldsymbol{d}}_{\mathrm{opt}}[k]$ and $\boldsymbol{d}[k]$, which can be written as

$$\underset{\boldsymbol{q}_f}{\text{minimize}} \ \mathbb{E}\left[\left\|\sum_{i=-K_w}^{K_w} \boldsymbol{Q}_f^{\mathsf{H}}\tilde{\boldsymbol{P}}_f[i]\boldsymbol{d}[k+i] - \boldsymbol{d}[k]\right\|^2\right]. \tag{49}$$

The decision variable is $\boldsymbol{q}_f$ because $\boldsymbol{Q}_f$ is uniquely determined by $\boldsymbol{q}_f$ following the relation in (30). Note that this MSE only accounts for the effects of the TX and RX filters, without the noise.

The objective function of the optimization problem (49) to find the optimal mismatched filter can be reformulated as

$$\mathbb{E}\left[\left\|\sum_{i=-K_w}^{K_w} \boldsymbol{Q}_f^{\mathsf{H}}\tilde{\boldsymbol{P}}_f[i]\boldsymbol{d}[k+i] - \boldsymbol{d}[k]\right\|^2\right]$$
$$= \mathrm{tr}\left(\sum_{i=-K_w}^{K_w} \boldsymbol{Q}_f^{\mathsf{H}}\tilde{\boldsymbol{P}}_f[i]\tilde{\boldsymbol{I}}_M\tilde{\boldsymbol{P}}_f[i]^{\mathsf{H}}\boldsymbol{Q}_f - \tilde{\boldsymbol{I}}_M\right) \tag{50a}$$
$$= \sum_{i=-K_w}^{K_w} \mathrm{tr}\left(\boldsymbol{Q}_f^{\mathsf{H}}\tilde{\boldsymbol{P}}_f[i]\tilde{\boldsymbol{I}}_M\tilde{\boldsymbol{P}}_f[i]^{\mathsf{H}}\boldsymbol{Q}_f - \delta[i]\tilde{\boldsymbol{I}}_M\right) \tag{50b}$$

$$= \sum_{i=-K_w}^{K_w} \left\| \boldsymbol{Q}_f^{\mathsf{H}} \tilde{\boldsymbol{P}}_f[i] \tilde{\boldsymbol{I}}_M - \delta[i] \tilde{\boldsymbol{I}}_M \right\|_{\mathrm{F}}^2 \tag{50c}$$

by using (5). Note that this can be also derived by using the bi-orthogonality condition of the TX and RX prototype filters [26]. Subsequently, we introduce some lemmas to simplify the optimization problem and find its solution.

Lemma 1: The matrix $\tilde{\boldsymbol{P}}_f[i]$ in (47) can be written as

$$\tilde{\boldsymbol{P}}_f[i] = \begin{bmatrix} (\tilde{\boldsymbol{C}}^0 \boldsymbol{W}_{\tilde{N}} \boldsymbol{E}[i] \boldsymbol{W}_N^{\mathsf{H}} \boldsymbol{p}_f)^{\mathsf{T}} \\ (\tilde{\boldsymbol{C}}^1 \boldsymbol{W}_{\tilde{N}} \boldsymbol{E}[i] \boldsymbol{W}_N^{\mathsf{H}} \boldsymbol{p}_f)^{\mathsf{T}} \\ \vdots \\ (\tilde{\boldsymbol{C}}^{M-1} \boldsymbol{W}_{\tilde{N}} \boldsymbol{E}[i] \boldsymbol{W}_N^{\mathsf{H}} \boldsymbol{p}_f)^{\mathsf{T}} \end{bmatrix}^{\mathsf{T}} \tag{51}$$

for $i = -K_w, -K_w + 1, \cdots, K_w$ in terms of $\boldsymbol{p}_f$.

Proof: For $n = 0, 1, \ldots, \tilde{N} - 1$, the $(n+1)$-th component of the first column of $\tilde{\boldsymbol{P}}_f[i]$ is given by

$$[\tilde{\boldsymbol{P}}_f[i]]_{n,0} = \sum_{l=0}^{\tilde{N}-1} [\boldsymbol{E}[i] \boldsymbol{p}_t]_l e^{-\mathrm{j}2\pi \frac{ln}{\tilde{N}}}, \tag{52}$$

from (3b) and (47). Then, for $n = 0, 1, \ldots, \tilde{N}-1$, the $(n+1)$-th component of the $(m+1)$-th column of $\tilde{\boldsymbol{P}}_f[i]$ is expressed as

$$[\tilde{\boldsymbol{P}}_f[i]]_{n,m} = \sum_{l=0}^{\tilde{N}-1} \left([\boldsymbol{E}[i] \boldsymbol{p}_t]_l e^{\mathrm{j}2\pi \frac{m(l-L_{\mathrm{add}})}{M}} \right) e^{-\mathrm{j}2\pi \frac{ln}{\tilde{N}}} \tag{53a}$$

$$= (-1)^{m(\tilde{K}-K)} [\tilde{\boldsymbol{P}}_f[i]]_{\mathrm{mod}\left(n-m\tilde{K}, \tilde{N}\right), 0}, \tag{53b}$$

similar to the proof of Proposition 1. Hence, the $(m+1)$-th column of $\tilde{\boldsymbol{P}}_f[i]$ is determined by applying a downward circular shift of $m\tilde{K}$ components to its first column and then multiplying by $(-1)^{m(\tilde{K}-K)}$. *hfill*□

Lemma 2: The matrix $\boldsymbol{Q}_f^{\mathsf{H}} \tilde{\boldsymbol{P}}_f[i]$ is a circulant matrix.

Proof: Using Proposition 1 and Lemma 1, for any $m, n \in \{0, 1, \cdots, M-1\}$ and $i \in \{-K_w, -K_w + 1, \cdots, K_w\}$, the $(n+1)$-th entry of the $(m+1)$-th row of $\boldsymbol{Q}_f^{\mathsf{H}} \tilde{\boldsymbol{P}}_f[i]$ can be written as

$$[\boldsymbol{Q}_f^{\mathsf{H}} \tilde{\boldsymbol{P}}_f[i]]_{m,n} = (\tilde{\boldsymbol{C}}^m \boldsymbol{q}_f)^{\mathsf{H}} (\tilde{\boldsymbol{C}}^n \boldsymbol{W}_{\tilde{N}} \boldsymbol{E}[i] \boldsymbol{W}_N^{\mathsf{H}} \boldsymbol{p}_f) \tag{54a}$$

$$= (\tilde{\boldsymbol{C}}^0 \boldsymbol{q}_f)^{\mathsf{H}} (\tilde{\boldsymbol{C}}^{n-m} \boldsymbol{W}_{\tilde{N}} \boldsymbol{E}[i] \boldsymbol{W}_N^{\mathsf{H}} \boldsymbol{p}_f) \tag{54b}$$

$$= [\boldsymbol{Q}_f^{\mathsf{H}} \tilde{\boldsymbol{P}}_f[i]]_{0, \mathrm{mod}(n-m, M)}, \tag{54c}$$

which is the $(\mathrm{mod}(n-m, M)+1)$-th entry of the first row of $\boldsymbol{Q}_f^{\mathsf{H}} \tilde{\boldsymbol{P}}_f[i]$. Thus, the $(m+1)$-th row is a rightward circular shift of the first row by m components, which implies that $\boldsymbol{Q}_f^{\mathsf{H}} \tilde{\boldsymbol{P}}_f[i]$ is a circulant matrix.*hfill*□

By using these lemmas, we can simplify the optimization problem (49) further as the following proposition. For that, we define

$$\Phi(\boldsymbol{p}_f, \boldsymbol{q}_f) \triangleq \sum_{i=-K_w}^{K_w} \left\| \tilde{\boldsymbol{P}}_f^{\mathsf{H}}[i] \boldsymbol{q}_f - \delta[i] \boldsymbol{e}_1 \right\|^2, \tag{55}$$

where $\delta[i]$ is the unit sample function, and $\tilde{\boldsymbol{P}}_f[i]$ is uniquely determined by the TX prototype vector $\boldsymbol{p}_f$ as specified in Lemma 1.

Proposition 4: The optimal solution of the optimization problem of the mismatched filter in (49) is equal to the optimal solution of the optimization problem given by

$$\underset{\boldsymbol{q}_f}{\text{minimize}} \ \Phi(\boldsymbol{p}_f, \boldsymbol{q}_f). \tag{56}$$

Proof: By using (50) and Lemma 2, we find that the squared Frobenius norm of $\boldsymbol{Q}_f^{\mathsf{H}} \tilde{\boldsymbol{P}}_f[i] \tilde{\boldsymbol{I}}_M - \delta[i] \tilde{\boldsymbol{I}}_M$ equals the squared norm of its first row multiplied by the number of nonzero rows of $\tilde{\boldsymbol{I}}_M$. This can be represented as

$$\sum_{i=-K_w}^{K_w} \left\| \boldsymbol{Q}_f^{\mathsf{H}} \tilde{\boldsymbol{P}}_f[i] \tilde{\boldsymbol{I}}_M - \delta[i] \tilde{\boldsymbol{I}}_M \right\|_{\mathrm{F}}^2$$

$$= \sum_{i=-K_w}^{K_w} (M - M_{\mathrm{null}}) \left\| \boldsymbol{e}_1^{\mathsf{T}} \left(\boldsymbol{Q}_f^{\mathsf{H}} \tilde{\boldsymbol{P}}_f[i] - \delta[i] \boldsymbol{I}_M \right) \right\|^2 \tag{57a}$$

$$= (M - M_{\mathrm{null}}) \Phi(\boldsymbol{p}_f, \boldsymbol{q}_f), \tag{57b}$$

where the first column of $\boldsymbol{Q}_f$ is equal to $\boldsymbol{q}_f$ from (30). □

Then, $\Phi(\boldsymbol{p}_f, \boldsymbol{q}_f)$ can be interpreted as the per-subcarrier MSE in the noiseless AWGN channel. The optimal RX prototype vector $\boldsymbol{q}_{f,\mathrm{opt}}(\boldsymbol{p}_f)$ as a function of $\boldsymbol{p}_f$ can be derived from solving the optimization problem (56) and is given by

$$\boldsymbol{q}_{f,\mathrm{opt}}(\boldsymbol{p}_f) = \left(\sum_{i=-K_w}^{K_w} \tilde{\boldsymbol{P}}_f[i] \tilde{\boldsymbol{P}}_f^{\mathsf{H}}[i] \right)^{-1} \left(\sum_{i=-K_w}^{K_w} \delta[i] \tilde{\boldsymbol{P}}_f[i] \boldsymbol{e}_1 \right)$$

$$= \left(\sum_{i=-K_w}^{K_w} \tilde{\boldsymbol{P}}_f[i] \tilde{\boldsymbol{P}}_f^{\mathsf{H}}[i] \right)^{-1} \tilde{\boldsymbol{P}}_f[0] \boldsymbol{e}_1. \tag{58}$$

Next, we demonstrate that minimizing our objective function is equivalent to maximizing the SIR. The SIR can be represented by

$$\mathrm{SIR} = \frac{\sum_{m=0}^{M-1} \left| [\boldsymbol{Q}_f^{\mathsf{H}} \tilde{\boldsymbol{P}}_f[0]]_{m,m} \right|^2}{\sum_{i=-K_w}^{K_w} \left\| \boldsymbol{Q}_f^{\mathsf{H}} \tilde{\boldsymbol{P}}_f[i] - \delta[i] \sum_{m=0}^{M-1} \boldsymbol{e}_{m+1} [\boldsymbol{Q}_f^{\mathsf{H}} \tilde{\boldsymbol{P}}_f[0]]_{m,m} \boldsymbol{e}_{m+1}^{\mathsf{T}} \right\|_{\mathrm{F}}^2} \tag{59}$$

because each diagonal entry of $\boldsymbol{Q}_f^{\mathsf{H}} \tilde{\boldsymbol{P}}_f[0]$ corresponds to the desired signal for each subcarrier in the frequency domain. Using Lemma 2, we can rewrite the SIR as

$$\mathrm{SIR} = \frac{\left| (\tilde{\boldsymbol{P}}_f[0] \boldsymbol{e}_1)^{\mathsf{H}} \boldsymbol{q}_f \right|^2}{\sum_{i=-K_w}^{K_w} \left\| \tilde{\boldsymbol{P}}_f^{\mathsf{H}}[i] \boldsymbol{q}_f - \delta[i] (\tilde{\boldsymbol{P}}_f[0] \boldsymbol{e}_1)^{\mathsf{H}} \boldsymbol{q}_f \boldsymbol{e}_1 \right\|^2}. \tag{60}$$

The minimum MSE (MMSE) per subcarrier in the noiseless AWGN channel can be obtained as

$$\mathrm{MMSE}_{\mathrm{NL}} = \Phi(\boldsymbol{p}_f, \boldsymbol{q}_{f,\mathrm{opt}}(\boldsymbol{p}_f))$$

$$= 1 - (\tilde{\boldsymbol{P}}_f[0] \boldsymbol{e}_1)^{\mathsf{H}} \left(\sum_{i=-K_w}^{K_w} \tilde{\boldsymbol{P}}_f[i] \tilde{\boldsymbol{P}}_f^{\mathsf{H}}[i] \right)^{-1} (\tilde{\boldsymbol{P}}_f[0] \boldsymbol{e}_1). \tag{61}$$

Similarly, the maximum SIR (MSIR) can be obtained by substituting $\boldsymbol{q}_{f,\mathrm{opt}}(\boldsymbol{p}_f)$ from (58) for $\boldsymbol{q}_f$ in the expression for SIR given in (60). This substitution leads to

$$\begin{aligned}\mathrm{MSIR} &= \frac{(\tilde{\boldsymbol{P}}_f[0]\boldsymbol{e}_1)^{\mathsf{H}}\left(\sum_{i=-K_w}^{K_w}\tilde{\boldsymbol{P}}_f[i]\tilde{\boldsymbol{P}}_f^{\mathsf{H}}[i]\right)^{-1}(\tilde{\boldsymbol{P}}_f[0]\boldsymbol{e}_1)}{1-(\tilde{\boldsymbol{P}}_f[0]\boldsymbol{e}_1)^{\mathsf{H}}\left(\sum_{i=-K_w}^{K_w}\tilde{\boldsymbol{P}}_f[i]\tilde{\boldsymbol{P}}_f^{\mathsf{H}}[i]\right)^{-1}(\tilde{\boldsymbol{P}}_f[0]\boldsymbol{e}_1)} \\ &= \frac{1}{\mathrm{MMSE}_{\mathrm{NL}}}-1 \end{aligned} \tag{62}$$

Therefore, the MSE minimization problem, with the objective function represented by $\Phi(\boldsymbol{p}_f, \boldsymbol{q}_f)$, is equivalent to the SIR maximization problem.

Given that the optimal RX prototype vector is determined by the TX prototype vector, the joint optimization problem involving both TX and RX prototype vectors can be reformulated into a single optimization problem with the TX prototype vector as the only decision variable. This can be represented by

$$\min_{\boldsymbol{p}_f,\,\boldsymbol{q}_f}\Phi(\boldsymbol{p}_f,\boldsymbol{q}_f) = \min_{\boldsymbol{p}_f}\min_{\boldsymbol{q}_f}\Phi(\boldsymbol{p}_f,\boldsymbol{q}_f) \tag{63a}$$

$$= \min_{\boldsymbol{p}_f}\Phi(\boldsymbol{p}_f,\boldsymbol{q}_{f,\mathrm{opt}}(\boldsymbol{p}_f)) \tag{63b}$$

To simplify the optimization process, the TX prototype vector $\boldsymbol{p}_f$ is given a specific structure, thereby reducing the number of free variables that need to be adjusted. Let $\boldsymbol{p}_f$ have consecutive N_{TX} nonzero components, beginning with the first component and alternating between adjacent components and their corresponding components from the end, where N_{TX} is an odd number to maintain its symmetry. This can be expressed as

$$\boldsymbol{p}_f^{\mathsf{T}}\boldsymbol{e}_{n+1}=0,\ \forall n\in\left\{\frac{N_{\mathrm{TX}}+1}{2},\cdots,N-\frac{N_{\mathrm{TX}}+1}{2}\right\}. \tag{64}$$

If N_{TX} increases, the spectrum of a subcarrier becomes broader, i.e., the FD localization of the TX prototype filter is reduced, while it provides greater flexibility to improve the SIR.

Moreover, the impulse response of the TX prototype filter must be real-valued. Hence, $\boldsymbol{p}_f$ must be complex conjugate-symmetric about its first component, which can be expressed as

$$\boldsymbol{p}_f^{\mathsf{T}}\boldsymbol{e}_{n+1}=(\boldsymbol{p}_f^{\mathsf{T}}\boldsymbol{e}_{N-n+1})^*,\ \forall n\in\left\{1,2,\cdots,\frac{N_{\mathrm{TX}}-1}{2}\right\}. \tag{65}$$

If one desires the impulse response to be symmetric, $\boldsymbol{p}_f$ must also be real symmetric about the first component. This structure makes the optimization problem simpler, as the number of free variables is nearly halved.

To maintain constant energy in the TX waveform, a constraint on the norm of the TX prototype vector, denoted by $\|\boldsymbol{p}_f\|^2 = 1$, is imposed. When designing the waveform, factors other than the SIR should also be considered. Such considerations will be integrated into the optimization problem as additional constraints, detailed as follows.

B. FALL-OFF RATE

To find a practical prototype filter, the FD localization of the filter must be considered. The FD localization of the TX prototype filter is significantly affected by the value of K. A large K implies that the filter has a long pulse, which enables a narrow spectrum and reduced out-of-band emission. However, this increases the overall computational complexity of the system in general. Also, N_{TX} can be reduced to make the spectrum narrower, but this decreases the SIR performance.

As another way to make the spectral confinement higher, we can impose a constraint on the fall-off rate of the spectrum of the TX prototype filter. The term *fall-off rate* refers to the rate of decay of the spectrum of the filter as the frequency approaches either positive or negative infinity. It is known that the fall-off rate can be restricted by imposing a certain constraint [16], [32] as follows. Define the column vector $\boldsymbol{\Psi}(R)$ as a function of a nonnegative integer R as

$$\boldsymbol{\Psi}(R)=\begin{bmatrix}\delta[R]\\ 1^R\\ 2^R\\ \vdots\\ (\frac{N}{2}-1)^R\\ (-\frac{N}{2})^R\\ \vdots\\ (-1)^R\end{bmatrix}. \tag{66}$$

In this column vector, the second to the $N/2$-th components are the R-th powers of integers from 1 to $N/2-1$. On the other hand, the $(N/2+1)$-th to the last components are the R-th powers of integers from $-N/2$ to -1. Then, for any nonnegative integer $R_{\max}$, if the condition expressed by

$$(\boldsymbol{\Psi}(R))^{\mathsf{T}}\boldsymbol{p}_f=0,\quad \forall R\in\{0,1,\cdots,R_{\max}\} \tag{67}$$

holds, then the decay rate of the spectrum of the prototype filter with FD vector $\boldsymbol{p}_f$ is at least as fast as $f^{-(R_{\max}+1)}$, where f is the frequency. The condition (67) is derived by imposing continuity on the R-th order derivative of the pulse [16], [32].

Note that the fall-off rate constraint only guarantees that the spectrum decreases at a certain rate for frequencies that are *far from* the center frequency. Hence, relying solely on the fall-off rate constraint does not ensure the capability of the filter to suppress out-of-band emission, meaning that both K and N_{TX} should be adjusted accordingly.

C. SNR LOWER BOUND

Maximizing the SIR only does not guarantee a high SINR. Hence, as previously shown in (45), the SNR lower bound is imposed as a constraint to ensure high SINR performance.

Let us denote the post-processing SNR as $\rho(\boldsymbol{p}_f, \boldsymbol{q}_f, \sigma^2)$, given the prototype vectors $\boldsymbol{p}_f$ and $\boldsymbol{q}_f$ in the AWGN channel with received SNR of σ^2. It can be written as

$$\rho(\boldsymbol{p}_f,\boldsymbol{q}_f,\sigma^2)=\frac{\left|(\tilde{\boldsymbol{P}}_f[0]\boldsymbol{e}_1)^{\mathsf{H}}\boldsymbol{q}_f\right|^2}{\sigma^2\left\|\tilde{\boldsymbol{P}}_f[0]\boldsymbol{e}_1\right\|^2\|\boldsymbol{q}_f\|^2} \tag{68a}$$

$$= \frac{\left|(\boldsymbol{W}_{\tilde{N}}\boldsymbol{E}[0]\boldsymbol{W}_N^{\mathsf{H}}\boldsymbol{p}_f)^{\mathsf{H}}\boldsymbol{q}_f\right|^2}{\sigma^2\|\boldsymbol{p}_f\|^2\|\boldsymbol{q}_f\|^2}. \tag{68b}$$

where Lemma 2 is used in the same way as in the derivation of (60). It can be rewritten as

$$\rho(\boldsymbol{p}_f, \boldsymbol{q}_f, \sigma^2) = \frac{1}{\sigma^2\|\boldsymbol{p}_f\|^2} \cdot \frac{\boldsymbol{q}_f^{\mathsf{H}}\boldsymbol{A}\boldsymbol{q}_f}{\boldsymbol{q}_f^{\mathsf{H}}\boldsymbol{q}_f}, \tag{69a}$$

where the matrix $\boldsymbol{A}$ is given by

$$\boldsymbol{A} = (\boldsymbol{W}_{\tilde{N}}\boldsymbol{E}[0]\boldsymbol{W}_N^{\mathsf{H}}\boldsymbol{p}_f)(\boldsymbol{W}_{\tilde{N}}\boldsymbol{E}[0]\boldsymbol{W}_N^{\mathsf{H}}\boldsymbol{p}_f)^{\mathsf{H}}. \tag{69b}$$

The matrix $\boldsymbol{A}$ is a Hermitian matrix, so that (69a) has the form of a Rayleigh quotient multiplied by a scalar value. Since the rank of $\boldsymbol{A}$ is 1 and one of its eigenvalues is $\|\boldsymbol{p}_f\|^2 = 1$, $\rho(\boldsymbol{p}_f, \boldsymbol{q}_f, \sigma^2)$ satisfies the inequality given by

$$\lambda_{\min} = 0 \le \sigma^2\rho(\boldsymbol{p}_f, \boldsymbol{q}_f, \sigma^2) = \rho(\boldsymbol{p}_f, \boldsymbol{q}_f, 1) \le 1 = \lambda_{\max}, \tag{70}$$

where $\lambda_{\min}$ and $\lambda_{\max}$ are the minimum and maximum eigenvalues of $\boldsymbol{A}$, respectively. We can then enforce an SNR constraint given by $\rho(\boldsymbol{p}_f, \boldsymbol{q}_f, 1) \ge 1 - \varepsilon$, where $\varepsilon > 0$ is a small value indicating the allowable SNR degradation. Note that the RX prototype vector has the value $\boldsymbol{q}_f = \boldsymbol{q}_{f,\text{opt}}(\boldsymbol{p}_f)$.

Adding the constraints we have discussed, the final optimization problem to find the optimal TX prototype vector is presented as

$$\underset{\boldsymbol{p}_f}{\text{minimize}}\ \Phi(\boldsymbol{p}_f, \boldsymbol{q}_{f,\text{opt}}(\boldsymbol{p}_f)) \tag{71a}$$

$$\text{subject to} \quad \|\boldsymbol{p}_f\|^2 = 1 \tag{71b}$$

$$(\boldsymbol{\Psi}(R))^{\mathsf{T}}\boldsymbol{p}_f = 0,\ \forall R \in \{0, \cdots, R_{\max}\} \tag{71c}$$

$$\rho(\boldsymbol{p}_f, \boldsymbol{q}_{f,\text{opt}}(\boldsymbol{p}_f), 1) \ge 1 - \varepsilon. \tag{71d}$$

Given the relation

$$\frac{1}{\text{SINR}_{\sigma^2}} = \frac{1}{\text{SIR}} + \frac{1}{\rho(\boldsymbol{p}_f, \boldsymbol{q}_{f,\text{opt}}(\boldsymbol{p}_f), \sigma^2)} \le \frac{1}{\text{SIR}} + \frac{\sigma^2}{1-\epsilon}, \tag{72}$$

where SINR_{σ^2} represents the SINR when the received SNR is σ^2, it becomes evident that maximizing the SIR correspondingly increases the SINR. By fixing N_{TX} and $R_{\max}$, we perform a line search on the value of ϵ to solve the optimization problem (71b). Note that increasing the lower bound of the post-processing SNR does not necessarily result in better performance, since the SIR may decrease with the increase of the lower bound. During each iteration, we ensure the resultant filters achieve satisfactory SIR or SINR values, allowing us to identify the best filter for the purpose. The RX prototype filter is then obtained as $\boldsymbol{q}_{f,\text{opt}}(\boldsymbol{p}_f)$ as given in (58).

TABLE 1. FD coefficients of proposed Tx prototype filters.

	$K=3, r=4/3$	$K=4, r=2$	
	Real	Real	Imaginary
$p_f[0]$	+1.0000	+1.0000	
$p_f[1]$	−0.7892	−0.9732	+0.3303
$p_f[2]$	+0.4181	+0.5568	−0.5615
$p_f[3]$	−0.0086	−0.0836	+0.2642
$p_f[4]$	−0.2447		
$p_f[5]$	+0.1244		

D. OPTIMIZED TX PROTOTYPE FILTERS

In this subsection, we present two TX prototype filters optimized by numerically solving (71b), each uniquely identified by the triplet $(K, r, M/S)$. The filter with $(K, r, M/S) = (3, 4/3, 16)$ consists of 11 FD taps, equivalent to 6 distinct taps due to symmetry, and is characterized by real symmetric FD coefficients. On the other hand, the filter with $(K, r, M/S) = (4, 2, 16)$ consists of 7 FD taps, equivalent to 4 distinct taps due to conjugate-symmetry, and is characterized by complex conjugate-symmetric FD coefficients. The coefficients for these TX prototype filters are presented in TABLE 1. These coefficients in the table have been normalized so that the center coefficient is equal to unity.

The applicability of the prototype filter is not restricted to a specific value of M. It can be employed across various values of M values, as long as the triplet combination of $(K, r, M/S)$ remains constant. For example, both filters can be used in a system with $M = 128$ and $S = 8$, as well as in a system with $M = 1024$ and $S = 64$.

V. NUMERICAL RESULTS

In this section, numerical results are presented to illustrate the performance of the proposed QAM-FBMC system. First, the computational complexity of the system is analyzed for distinct TX and RX structures, specifically, the direct FD and PPN-based structures. Next, the filter responses and power spectral density (PSD) of the proposed system are examined, and a comparison is made with those of other QAM-FBMC systems. Lastly, a comparative evaluation is conducted on the performance of the proposed system with those of the CP-OFDM, OQAM-FBMC, and QAM-FBMC systems, focusing on the SIR, the SINR, and the bit-error rate (BER).

A. COMPUTATIONAL COMPLEXITY

In this subsection, we provide a detailed examination of the computational complexity of the TX and RX structures of the proposed QAM-FBMC system. The structures analyzed include the direct FD structure and the proposed PPN-based structure. The complexity is analyzed on a per FBMC symbol basis, which means that the complexity covers the generation of a single FBMC symbol at the TX and the processing of a single FBMC symbol at the RX. We provide the complexity in terms of big O notation, along with the numbers of real additions and multiplications. We illustrate the numbers of real additions and multiplications between the systems with each of the structures of the proposed system

TABLE 2. Computational complexity of Txs.

TX Structure	Computational Complexity
Direct FD	$O(N_{\mathrm{TX}}M + KM\log KM)$
PPN-based	$O(KM + M\log M)$

and the low-complexity system in [26]. For this analysis, we assume that we have a perfect estimate of the channel impulse response in advance, excluding the complexity of the channel estimator, as it is beyond the scope of this paper. In accordance with the split-radix FFT presented in [33], the numbers of real additions and multiplications required for an M-point FFT amount to $(3M\log_2 M - 3M + 4)$ and $(M\log_2 M - 3M + 4)$, respectively. In this analysis, we use KM and rKM for N and $\tilde{N}$, respectively, to conveniently compare the complexity.

1) COMPLEXITY OF TX

In the analysis of TX complexity, the number of nonzero FD components in the TX prototype filter is denoted by N_{TX}. As an example, for the PHYDYAS filter with $K = 4$, this value is equal to 7, since we count the components on both sides of the filter, not just one side.

We first analyze the complexity in terms of the big O notation. The TX with the direct FD structure consists of the FD filter $\boldsymbol{P}_f$ and the KM-point inverse fast Fourier transform (IFFT). The complexity of the FD filter, derived from the multiplication of N_{TX} nonzero FD coefficients and M QAM symbols, is $O(N_{\mathrm{TX}}M)$. The complexity of the KM-point IFFT is $O(KM\log KM)$. As a result, the total complexity of the direct FD structure can be expressed as $O(N_{\mathrm{TX}}M + KM\log KM)$.

On the other hand, the TX with the PPN-based structure consists of the M-point IFFT, a circular shift operation with postfix insertion, and the summation of vectors resulting from the Hadamard product. The complexity of the M-point IFFT amounts to $O(M\log M)$. The complexity of the circular shift operation, the Hadamard product, and the summation is $O(KM)$. Consequently, the total complexity of the PPN-based structure is $O(KM + M\log M)$. These total complexities are summarized in TABLE 2 using the big O notation.

Next, we analyze the complexity in terms of the numbers of real additions and multiplications. For the direct FD structure, two main operations are performed serially. The FD filter requires $N_{\mathrm{TX}}(M-1)$ complex additions and $N_{\mathrm{TX}}M$ complex multiplications, equivalent to $4N_{\mathrm{TX}}M - 2M$ real additions and $4N_{\mathrm{TX}}M$ real multiplications. Following this, the KM-point IFFT requires $(3KM\log_2 KM - 3KM + 4)$ real additions and $(KM\log_2 KM - 3KM + 4)$ real multiplications. Hence, the total numbers of real additions and multiplications for the direct FD structure can be expressed as

$$\mathfrak{A}_{\mathrm{TX,direct}} = 4N_{\mathrm{TX}}M + 3KM\log_2 KM - 3KM - 2M + 4, \quad (73a)$$

$$\mathfrak{M}_{\mathrm{TX,direct}} = 4N_{\mathrm{TX}}M + KM\log_2 KM - 3KM + 4, \quad (73b)$$

respectively.

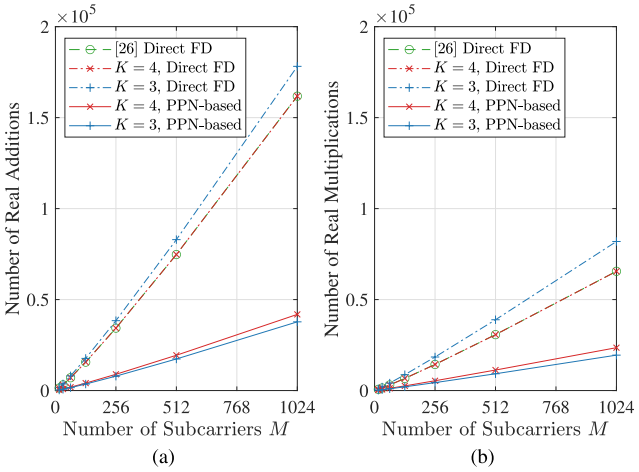

FIGURE 5. Numbers of (a) real additions and (b) real multiplications of different TXs.

For the PPN-based structure, three main operations are performed serially. The M-point IFFT requires $(3M\log_2 M - 3M + 4)$ real additions and $(M\log_2 M - 3M + 4)$ real multiplications. Following this, the circular shift operation requires $(K-1)$ real multiplications. Then, the Hadamard product and the summation require $(KM - M - S)$ complex additions and KM complex multiplications, equivalent to $(4KM - 2M - 2S)$ real additions and $4KM$ real multiplications. Therefore, the total numbers of real additions and multiplications for the PPN-based structure can be expressed as

$$\mathfrak{A}_{\mathrm{TX,PPN}} = 3M\log_2 M + 4KM - 5M - 2S + 4, \quad (74a)$$

$$\mathfrak{M}_{\mathrm{TX,PPN}} = M\log_2 M + 4KM - 3M + K + 3, \quad (74b)$$

respectively.

FIGURE 5-(a) and 5-(b) illustrate comparisons of five systems in terms of the number of real additions and the number of real multiplications, respectively. Two systems with the proposed filters, each with $K = 3$ and $K = 4$, are implemented with the direct FD structure. Likewise, another two systems with the proposed filters, each with $K = 3$ and $K = 4$, are implemented with the PPN-based structure. The system from [26] is implemented only with the direct FD structure. The IFFT requires its size to be a power of two for efficiency. When the size of the IFFT is not a power of two, the size is adjusted upwards to the nearest power of two for representation in the figure.

Interestingly, the complexity of the system with $K = 3$ is higher than that of the system with $K = 4$ when using the direct FD structure. The reason for this is that the prototype filter with $K = 3$ has 11 taps, more than the 6 taps of the prototype filter with $K = 4$. However, when using the PPN-based structure, the complexity of the system with $K = 3$ is slightly lower than that of the system with $K = 4$ since it is not affected by the number of nonzero FD components in the prototype filter.

The PPN-based structure substantially reduces the TX computational complexity of both systems, reducing the

TABLE 3. Computational complexity of RXs.

RX Structure	Computational Complexity
Direct FD	$O(N_{\mathrm{RX}}M + rKM \log rKM)$
PPN-based	$O(rKM \log rKM)$

numbers of real additions and of real multiplications to about one-third or even less than those of the direct FD structure. This reduction is primarily attributed to the fact that the direct FD structure has a KM-point IFFT, with a complexity of $O(KM \log KM)$, whereas the PPN-based structure has an M-point IFFT, with a complexity of $O(M \log M)$.

2) COMPLEXITY OF RX

In the analysis of RX complexity, the number of nonzero FD components in the RX prototype filter is denoted by N_{RX}. Each RX in this analysis has an FD one-tap equalizer placed before the FD filter. This structure divides the RX into three parts: the FFT, the FD channel equalizer, and the FD filter. The direct FD and PPN-based structures share the same FFT and FD one-tap LMMSE equalizer, but they use different FD filters.

As stated at the end of Section III, further complexity reduction for the PPN structure is achievable by positioning the equalizer after the RX filter. However, this may negatively impact the RX performance, despite its complexity benefits. This concern is further evidenced by the BER comparison in frequency selective channels, discussed in a later subsection. Hence, the proposed system does not adopt this structure and its complexity is not further discussed in this paper.

In terms of the big O notation, the analysis begins with an examination of the components that are common to both structures. The complexity of the rKM-point FFT is $O(rKM \log rKM)$. The complexity of the FD one-tap equalizer, which includes acquiring $\hat{\boldsymbol{H}}_f[k]$ from the estimated channel impulse vector, is also $O(rKM \log rKM)$ [11], [26].

Now, we consider the FD filter, where the complexity varies between the two structures: the direct FD structure and the PPN-based structure. The direct FD structure has a filtering complexity of $O(N_{\mathrm{RX}}M)$. Meanwhile, the PPN-based structure, which includes the rKM-point IFFT at the beginning, has a complexity of $O(rKM + rKM \log rKM)$. The total complexities, which include the common components, are summarized in TABLE 3 using the big O notation.

As a special case, when a full-tap RX prototype filter with $N_{\mathrm{RX}} = rKM$ is used, the complexity of the direct FD structure becomes $O(rKM^2 + rKM \log rKM)$. This reflects a quadratic relationship with M, unlike the PPN-based structure, which exhibits a log-linear complexity relationship with M. Furthermore, it is notable that the LMMSE RX, as described in [18], has a complexity of $O(K^3M^3)$, indicating a cubic relationship with M, due to the matrix inversion. This complexity can impose a substantial computational burden, especially for large values of M.

The analysis of the numbers of real additions and multiplications begins with an examination of the components

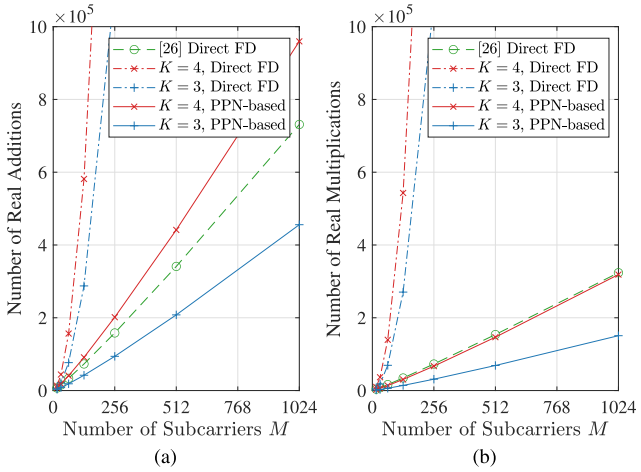

FIGURE 6. Numbers of (a) real additions and (b) real multiplications of different RXs including the common components.

common to both structures. The foremost rKM-point FFT requires $(3rKM \log_2 rKM - 3rKM + 4)$ real additions and $(rKM \log_2 rKM - 3rKM + 4)$ real multiplications. Assuming that the channel impulse response is already provided, and excluding the complexity of acquiring the channel impulse response, the FD channel estimation requires an rKM-point FFT with additional L_{ch} real additions and $3L_{\mathrm{ch}}$ real multiplications. The total complexity for channel estimation amounts to $(3rKM \log_2 rKM - 3rKM + L_{\mathrm{ch}} + 4)$ real additions and $(rKM \log_2 rKM - 3rKM + 3L_{\mathrm{ch}} + 4)$ real multiplications. The subsequent one-tap equalization requires rKM complex multiplications, which are equivalent to $2rKM$ real additions and $4rKM$ real multiplications.

Focusing on the filtering processes, we analyze the numbers of real additions and multiplications required in both the direct FD structure and the PPN-based structure. The former uses a more direct method, whereas the latter involves multiple procedures.

In the direct FD structure, the filtering requires $(N_{\mathrm{RX}} - 1)M$ complex additions and $N_{\mathrm{RX}}M$ complex multiplications. This is equivalent to the numbers of real additions and multiplications expressed as

$$\mathfrak{A}_{\mathrm{RX,direct}} = 4N_{\mathrm{RX}}M - 2M, \tag{75a}$$

$$\mathfrak{M}_{\mathrm{RX,direct}} = 4N_{\mathrm{RX}}M, \tag{75b}$$

respectively. At first glance, the values might be perceived as being low. However, when a full-tap RX prototype filter is used, i.e., $N_{\mathrm{RX}} = rKM$, they become $\mathfrak{A}_{\mathrm{RX,direct}} = 4rKM^2 - 2M$ and $\mathfrak{M}_{\mathrm{RX,direct}} = 4rKM^2$, making the RX with a full-tap RX prototype filter less practical.

In the PPN-based structure, the filtering process involves three steps: the rKM-point IFFT, the Hadamard product combined with summation and circular shift, and the M-point FFT. The rKM-point IFFT requires $(3rKM \log_2 rKM - 3rKM + 4)$ real additions and $(rKM \log_2 rKM - 3rKM + 4)$ real multiplications. The Hadamard product and summation with circular shift require $(rKM - M)$ complex

additions, rKM complex multiplications, and additional $(K_u + K_w - 1)$ real multiplications, which are equivalent to $(4rKM - 2M)$ real additions and $(4rKM + K_u + K_w - 1)$ real multiplications. Lastly, the M-point FFT requires $(3M \log_2 M - 3M + 4)$ real additions and $(M \log_2 M - 3M + 4)$ real multiplications. Thus, overall, the filtering process in the PPN-based structure requires total numbers of real additions and multiplications expressed as

$$\mathfrak{A}_{\mathrm{RX,PPN}} = 3rKM \log_2 rKM + 3M \log_2 M + rKM - 5M + 8, \quad (76a)$$

$$\mathfrak{M}_{\mathrm{RX,PPN}} = rKM \log_2 rKM + M \log_2 M + rKM - 3M + K_u + K_w + 7, \quad (76b)$$

respectively.

FIGURE 6-(a) and 6-(b) illustrate comparisons of five systems, similar to those in the TX complexity comparison. For illustration purposes, the complexity of the common components of the RXs is included, and $K_u + K_w = rK + 1$ is used. The FFT and IFFT sizes are rounded up to the nearest power of two if they are not already a power of two.

When using our proposed filters with $K = 3$ and $K = 4$, the systems with the direct FD structure demonstrate significantly higher computational complexity than those with the PPN-based structure. This increase in complexity primarily arises from the quadratic relationship of the full-tap RX prototype filter with M. Consequently, using a full-tap filter makes the systems implemented with the direct FD structure impractical.

When implemented with the PPN-based structure, the system with the proposed filter of $K = 4$ becomes viable, exhibiting a complexity similar to the system implemented with the direct FD structure in [26]. Specifically, the number of real additions of the proposed system with $K = 4$ exceeds that of the system in [26], whereas the number of real multiplications is slightly lower. Interestingly, the system with the proposed filter of $K = 3$, when implemented with the PPN-based structure, shows roughly half the RX complexity of the system in [26]. The primary reason for this reduction lies in the significance of the rKM-point FFT and IFFT to the complexity. The value of rKM of the system with $K = 3$ is half of the value of the system with $K = 4$, thus halving the size of FFT or IFFT.

B. TX FILTER RESPONSES

In this subsection, we examine both the impulse response and PSD of the proposed systems, specifically incorporating the proposed filters with $K = 3$ and $K = 4$.

1) IMPULSE RESPONSE

FIGURE 7 illustrates the impulse responses $p_0(t)$ of the proposed filters, corresponding to distinct K values, where T_s represents the FBMC symbol period. Each impulse response shown in the figure spans a single pulse duration. Since the length of one FBMC symbol is KM in the discrete time, the filter with $K = 3$ is shorter in representation than the one with

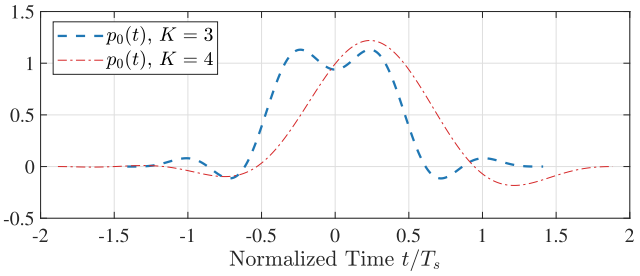

FIGURE 7. Impulse responses of the TX filters of the proposed systems with different values of K.

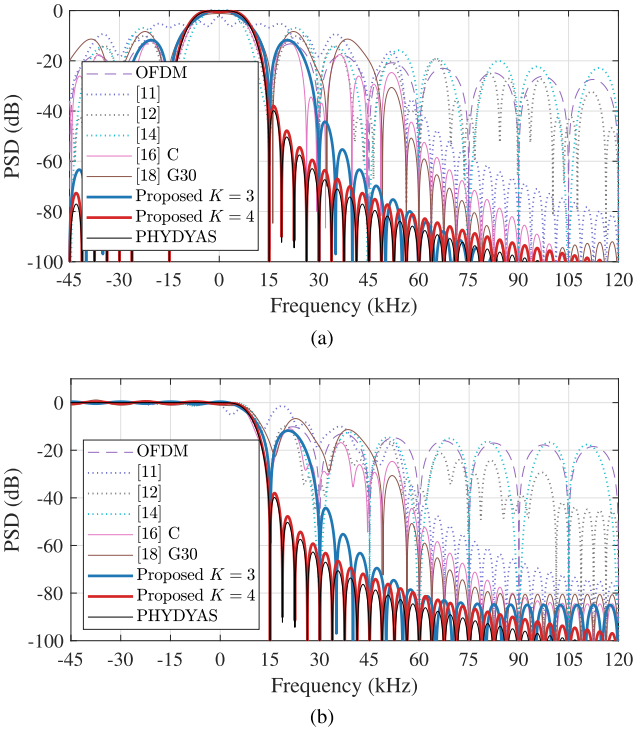

FIGURE 8. (a) Per-subcarrier PSDs and (b) overall PSDs of the OFDM and QAM-FBMC systems when $M = 1024$ and $M_{\mathrm{null}} = 424$.

$K = 4$. While the prototype filter with $K = 3$ demonstrates symmetry about its center due to its real symmetric FD taps, the filter with $K = 4$ is asymmetrical, having complex conjugate-symmetric FD taps. The shorter length of the filter with $K = 3$, coupled with the low-complexity RX as shown in the previous subsection, makes it more suitable for applications with stricter latency requirements.

2) PSD

FIGURE 8-(a) and 8-(b) present the per-subcarrier and overall PSDs of OFDM and QAM-FBMC systems, with the subcarrier spacing $F_{\mathrm{SC}} = 15$ kHz, $M = 1024$, and $M_{\mathrm{null}} = 424$. For the QAM-FBMC systems with a pair of TX prototype filters in [12] and [14], average PSD values are shown in FIGURE 8(a). For this and subsequent subsections, the Case C filter from [16] and the Type G30 filter from [18] are included in the numerical results. Regarding the fall-off

rate constraint, the proposed filters have been optimized using parameters ($K = 3, R_{\max} = 3$) and ($K = 4, R_{\max} = 1$).

FIGURE 8-(a) shows that the systems with a pair of TX prototype filters [11], [12], [14] have relatively high out-of-band emission. For these systems, one of the pair of filters has small side lobes, but the other has large side lobes. This makes the average spectrums of the systems relatively wide and increases the out-of-band emission. In particular, the system in [14] has large side lobes, whose overall out-of-band emission is worse than those of the OFDM system. On the other hand, the systems with a single TX prototype filter in [16] and [18] have a relatively narrow spectrum, but their side lobes are larger than those of the proposed systems. The system in [26] uses the PHYDYAS filter, which has the narrowest spectrum and smallest side lobes compared to the other systems. The proposed system with $K = 4$ exhibits a spectrum closely resembling that of the system employing the PHYDYAS filter. The proposed system with $K = 3$ has a wider per-subcarrier spectrum than that of the PHYDYAS filter, which is attributed to its larger number of FD taps. However, its out-of-band emission is small thanks to the rapid fall-off rate utilized in the filter optimization. Among the compared FBMC and OFDM systems, the FBMC system with the PHYDYAS filter and the proposed systems demonstrate superior spectral confinement.

FIGURE 8-(b) shows similar results, where each of the PSDs is effectively the sum of 600 per-subcarrier PSDs. Although the fall-off rate constraint used to optimize the proposed filter with $K = 3$, which is $R_{\max} = 3$, is stricter than the rate used to optimize the filter with $K = 4$, which is $R_{\max} = 1$, the filter with $K = 4$ has a higher K, which leads to a more spectrally confined filter in the figure.

The primary reasons for the proposed systems having low out-of-band emission are not only the use of the fall-off rate constraint in filter optimization but also the small number of FD taps in the TX prototype filter. This small number of FD taps is achievable by employing a mismatched RX filter, which is not a feasible approach for conventional QAM-FBMC systems with matched filters. Since the spectrum of a system is solely determined by the TX prototype filter, the number of FD taps of the TX prototype filter can be kept small and, instead, the number of the FD taps of the RX prototype filter can be increased to improve other performance metrics.

We can determine the required number of guard subcarriers based on the number of subcarriers needed to bring the PSD to a certain level, for instance, below -30 dB. Guard subcarriers can be crucial for scenarios like asynchronous multi-user communications. Specifically, the system with the PHYDYAS filter [26] and the proposed system with $K = 4$ each require two guard subcarriers, one on each frequency side. On the other hand, the proposed system with $K = 3$ requires four guard subcarriers, two for each frequency side. The other QAM-FBMC systems presented in FIGURE 8-(b) demand at least 8 guard subcarriers. Such spectral characteristics emphasize the suitability of the proposed system with $K = 4$ for applications demanding strict spectral requirements.

TABLE 4. SIR of FBMC systems.

	TX Prototype Filter	RX Filter	SIR	Approx. EVM
[11]	Pair	Matched	19.4 dB	10.7%
[12]	Pair	Matched	20.4 dB	9.5%
[14]	Pair	Matched	65.2 dB	0.05%
[16] C	Single	Matched	17.4 dB	13.3%
[18] G30	Single	LMMSE	25.9 dB	5.1%
[26]	Single	Mismatched	29.5 dB	3.3%
Proposed $K = 3$	Single	Mismatched	43.5 dB	0.7%
Proposed $K = 4$	Single	Mismatched	80.1 dB	0.01%

The proposed TX prototype filters have a main lobe wider than the Nyquist minimum bandwidth, resulting in each signal transmitted by each subcarrier exhibiting cyclostationarity [34]. Consequently, the proposed RX prototype filter should have large peaks in the time domain and large side lobes in the frequency domain to effectively exploit temporal and spectral correlation for self-interference suppression. This rationale justifies not only the extension of the RX filter length but also the removal of the sparsity constraint in the FD taps during RX prototype filter optimization, which may reduce self-interference, as will be demonstrated in the following subsections.

C. SIR AND EVM

In this subsection, the SIR and error-vector magnitude (EVM) performance of QAM-FBMC systems is compared. The EVM serves as a metric to measure system imperfections, such as filter flaws and nonlinear distortions [35]. In this paper, we define the approximate EVM, denoted by $\mathrm{EVM}_{\mathrm{approx}}$, as the average EVM for each symbol based on the noiseless AWGN channel MSE, denoted by $\mathrm{MSE}_{\mathrm{NL}}$. The approximate EVM can be expressed as

$$\mathrm{EVM}_{\mathrm{approx}} = \sqrt{\mathrm{MSE}_{\mathrm{NL}}} = \frac{1}{\sqrt{\mathrm{SIR} + 1}}, \tag{77}$$

similar to (62). The SIR for the proposed system is expressed as (60).

TABLE 4 presents the SIR and approximate EVM values of the QAM-FBMC systems discussed in the paper when $M = 1024$. It can be shown that other systems with completely different combinations of system parameters, including the value of M, also exhibit almost the same trend, but they are not compared here in the interest of fairness. TABLE 4 shows that the QAM-FBMC systems that utilize the matched filter at the RX [11], [12], [16] generally exhibit relatively low SIR values, with the exception of the system in [14], which has a high SIR value of 65.2 dB. This value is equivalent to the SIR value of the OQAM-FBMC system that employs the PHYDYAS filter. Despite its high SIR value, the system described in [14] is characterized by large out-of-band emission that surpasses those commonly found in OFDM systems as illustrated in Fig 8. If we compare the

spectrum and SIR performance among the systems with a matched RX filter and unit TF symbol density [11], [12], [14], [16], as shown in FIGURE 8-(a) and TABLE 4, a trade-off between SIR and out-of-band emission performance becomes evident. In general, systems with a higher SIR value have a wider spectrum and higher out-of-band emission. This trade-off is derived from the Balian-Low theorem, which states that excellent orthogonality and TF localization cannot be achieved simultaneously with the symbol density of unity.

On the other hand, TABLE 4 shows that the QAM-FBMC system with the LMMSE RX [18] achieves a higher SIR than QAM-FBMC systems that have a matched RX filter. By using the mismatched filter, it relaxes the TF localization only at the RX, which results in overall better SIR and out-of-band emission performance than the systems with the matched RX filter. Nonetheless, it has a higher complexity and its SIR values still fall short compared to those of the proposed systems. The system in [26] not only uses the mismatched RX filter but also increases the TF-product and the RX observation window, which further improves the SIR and out-of-band emission performance. However, the number of FD taps in the RX prototype filter is constrained to maintain low complexity, which limits the performance improvement.

The proposed systems with the mismatched filter at the RX achieve even higher SIR values compared to the system presented in [26]. Unlike the system in [26], which does not use the PPN-based structure, the proposed system utilizes it. Hence, the limitation of the system in [26] is overcome without a significant increase in complexity, as previously demonstrated in the complexity analysis. Thus, the proposed system with $K = 4$ achieves the highest SIR among all the QAM-FBMC systems discussed in this paper, and the proposed system with $K = 3$ also offers an excellent SIR value while maintaining a complexity lower than that of the proposed system with $K = 4$. Note that as the overlapping factor increases, achieving a higher SIR becomes easier because it becomes easier to achieve high spectral confinement so that there is more room to increase the SIR.

As noted in their respective papers, systems with a unit TF symbol density and a matched RX filter, but with different combinations of system parameters [15], [17], [23], show almost the same trend, having SIR values of less than 20 dB. On the other hand, the systems in [25] have a relaxed TF symbol density and a matched RX filter. One of these systems achieves a high SIR value of 46.8 dB with $TF = 1.0625$ and $K = 32$, but no filter supporting high-order modulations is found with a lower K value with this system design [25].

Recall that the EVM requirements by the standards are about 8% to support 64-QAM, 3.5% to support 256-QAM, 2.5% to support 1024-QAM [36]. Most of the compared QAM-FBMC systems do not satisfy the EVM requirements for 256-QAM. It is noteworthy that the systems presented in [25], according to their findings, support 256-QAM with a relaxed TF symbol density. However, due to their high $K = 16$ or 32, these systems are particularly suited for use cases involving a smaller number of subcarriers, such as multi-user uplink scenarios with $M = 16$. On the other hand, both proposed systems achieve an approximate EVM of less than 1%, which is sufficient to support 1024-QAM, provided that channel distortion or noise is not significant. Hence, the proposed systems may be used for future applications requiring high-order modulations. Overall, by slightly increasing the TF-product and relaxing the time and frequency localization only of the RX filter, QAM-FBMC systems can attain both high SIR and low out-of-band emission simultaneously, while maintaining low complexity through the use of the proposed PPN-based structure.

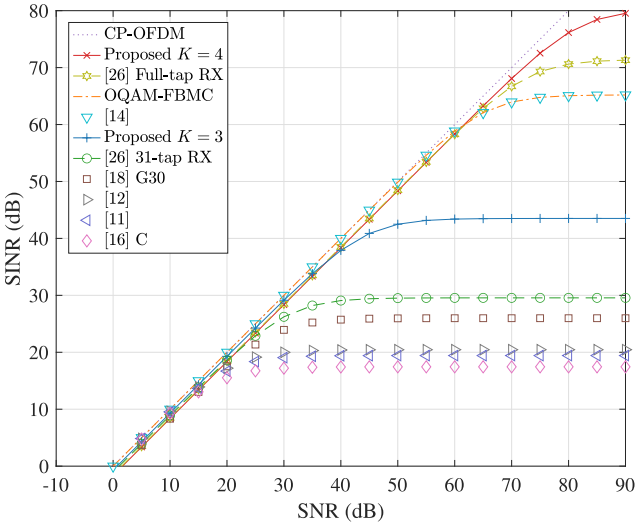

FIGURE 9. SINR in the AWGN channel when $M = 1024$ and $M_{\text{null}} = 424$.

D. SINR

In this subsection, we compare the SINR of the proposed systems with other systems. FIGURE 9 illustrates the SINR performance in the AWGN channels. Analytically, the SINR approaches the SIR as the SNR increases and saturates at the SIR value. Since the CP-OFDM system does not have self-interference, its SINR is equal to its SNR. The figure in this analysis closely aligns with the SIR comparison presented in TABLE 4.

In FIGURE 9, the proposed system with $K = 3$ demonstrates excellent performance for SNR values less than 40 dB, and the proposed system with $K = 4$ exhibits similar performance for SNR values less than 70 dB. In particular, the proposed system with $K = 3$ performs the best among the compared QAM-FBMC systems except [14] in the low SNR regime. In conditions of extremely high SNR, the proposed system with $K = 4$ proves to be the superior performer among all the QAM-FBMC systems. Interestingly, the proposed system with $K = 3$ shows higher SINR values than those of the proposed system with $K = 4$ in the low SNR regime. This is because the proposed prototype filter with $K = 4$ is an optimization result with a less strict post-processing SNR constraint to achieve a higher

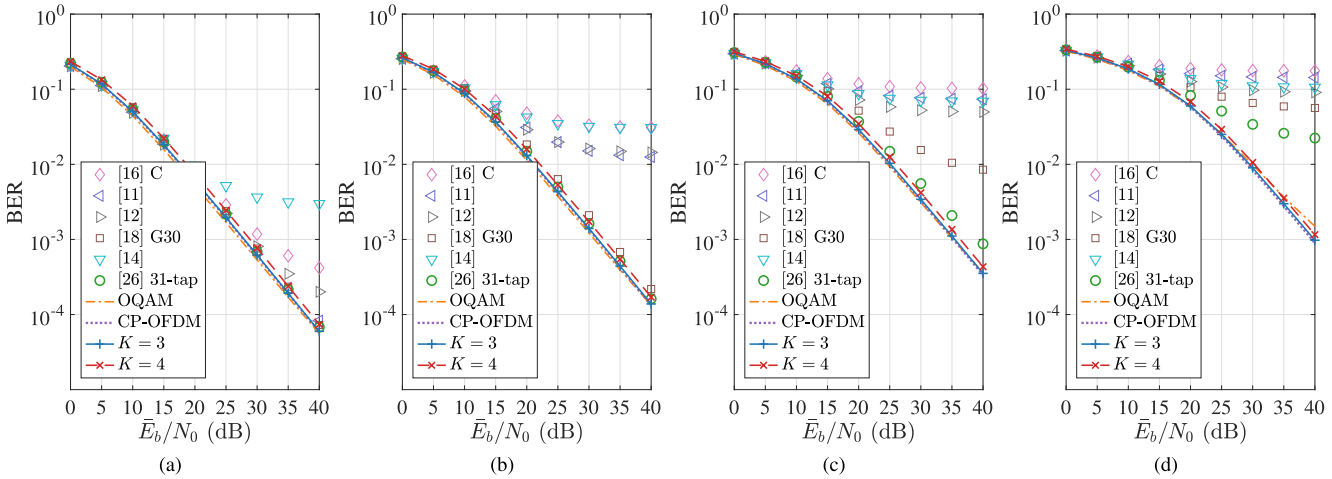

FIGURE 10. BER in the EPA channel when $M = 1024$ and $M_{\text{null}} = 424$ with (a) 16-QAM, (b) 64-QAM, (c) 256-QAM, and (d) 1024-QAM data symbols.

SIR value. Remarkably, our proposed system with $K = 4$ surpasses the performance of the full-tap RX prototype filter system in [26] in the high SNR regime, an achievement made possible by jointly optimizing the TX and RX prototype filters. As mentioned in [26], the system with its full-tap RX prototype filter is not considered practical for real-world applications. In contrast, the systems with a full-tap RX prototype filter proposed in this paper are feasible solutions for practical use by using the proposed PPN-based structure.

E. BER

In this subsection, we compare the BER performance of the proposed systems with other systems. For the BER analysis, we assume a perfect channel impulse response estimate at the RX. All QAM-FBMC systems employ FD one-tap equalizers, except for the system using the LMMSE RX in [18]. The OQAM-FBMC system and the QAM-FBMC system in [14] place the FD one-tap equalizer *after* the RX filter, whereas other QAM-FBMC systems place it *before*. The TF-product of the CP-OFDM system is approximately 1.07 due to CP overhead.

FIGURE 10 illustrates the uncoded BER performance in frequency-selective channels using the Extended Pedestrian A (EPA) model, as described in [36], with 7 taps and a maximum delay spread of 0.410 μs. Mostly, the QAM-FBMC systems with higher SINR performance in FIGURE 9 show lower BER performance in FIGURE 10. The exception is that the system in [14] exhibits poor BER performance despite its very high SIR and SINR in the AWGN channels. This is because it has very high out-of-band emission and equalization after filtering is not effective in frequency-selective channels, especially for the system whose spectrum is not well-localized. In such a case, non-equalized subcarriers may affect the filtering process with severe interference. The proposed system with $K = 3$ exhibits nearly optimal BER performance in both types of transmissions. The proposed system with $K = 4$ shows similar performance but with a slightly higher BER because of its less strict post-processing SNR constraint used in the filter optimization, as pointed out in the previous subsection.

The QAM-FBMC systems with matched RX filters [11], [12], [16] only show comparable BER for 4-QAM transmissions in these channels. On the other hand, the LMMSE-RX system in [18] and mismatched-RX system in [26] show great BER performance up to 16-QAM transmissions and 64-QAM transmissions, respectively. Among the compared QAM-FBMC systems, only the proposed systems properly support 1024-QAM in the EPA channel as FIGURE 10-(d) shows. This is implied by the comparison of the approximate EVM in TABLE 4, where only the proposed systems have the approximate EVM less than 2.5%.

FIGURE 11 illustrates the uncoded BER performance in frequency-selective channels following the Typical Urban (TU) model, as described in [37], incorporating 20 taps and a maximum delay spread of 2.140 μs. FIGURE 11 shows a more pronounced performance gap between the systems than those in the EPA channels. The proposed system with $K = 4$ shows outstanding performance among the QAM-FBMC systems, especially at a high SNR regime, whereas the system with $K = 3$ also exhibits excellent BER performance for SNR values ≤ 35 dB.

Both systems also exceed the OQAM-FBMC system with the PHYDYAS filter performance for SNR values $\geq$ 25 dB. The OQAM-FBMC system shows worse BER performance in this SNR range, which is different from the results presented in FIGURE 10. This difference is due to the greater frequency selectivity of the TU channels compared to the EPA channels, making equalization after filtering less effective. On the other hand, the proposed system has an FD one-tap equalizer before the RX filter for high performance in highly frequency-selective channels. For 64-QAM transmissions, the QAM-FBMC system employing the LMMSE RX [18] can outperform the proposed system with $K = 3$ that uses one-tap equalizers in highly

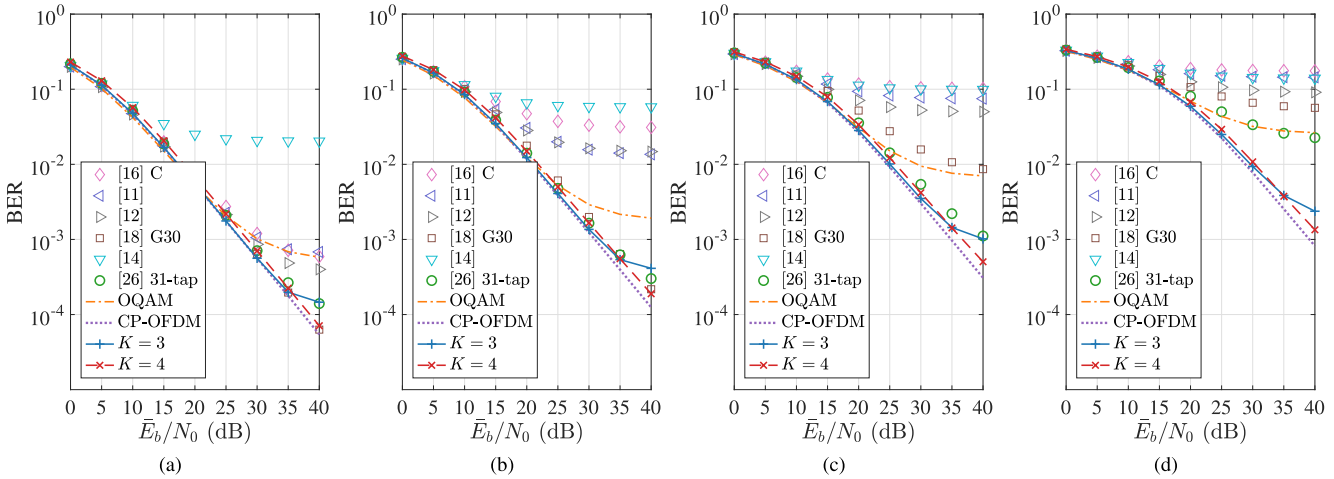

FIGURE 11. BER in the TU channel when $M = 1024$ and $M_{\text{null}} = 424$ with (a) 16-QAM, (b) 64-QAM, (c) 256-QAM, and (d) 1024-QAM data symbols.

frequency-selective channels. However, this comes at the expense of the high complexity associated with the full-tap LMMSE, and its BER performance is worse than that of the proposed systems for higher-order transmissions than 64-QAM. The proposed systems with high SIR performance support high-order modulations better than the other QAM-FBMC systems, even up to 1024-QAM.

VI. CONCLUSION

In this paper, we have proposed QAM-FBMC systems with the PPN-based structure and jointly optimized TX and RX prototype filters. At the RX, they employ the FD one-tap LMMSE equalizer followed by the fixed mismatched filter. The proposed PPN-based structure accommodates QAM-FBMC systems with not only the decreased TF symbol density but also the extended observation window. The proposed TX and RX prototype filters are jointly optimized to maximize the approximate SINR under the fall-off rate constraint.

While QAM-FBMC systems are known for high spectral efficiency and low out-of-band emission, they encounter challenges in achieving high spectral confinement and low self-interference simultaneously, which stems from the Balian-Low theorem. This paper overcomes these challenges by relaxing the TF localization at the RX, specifically extending the observation window and removing the constraint on the filter sparsity, in addition to relaxing TF symbol density slightly. The resulting systems not only achieve significantly reduced self-interference and high spectral confinement but also maintain low complexity by using the proposed PPN-based structure, as evidenced by our numerical evaluations. An important advantage of the proposed systems is their capability to support high-order modulations like 1024-QAM with low complexity, achieved by avoiding a high-complexity RX, such as full-tap LMMSE or IIC, and without increasing the overlapping factor. This is particularly significant as it facilitates higher data rates and more efficient spectrum utilization without necessitating complex receiver designs, which are often the bottleneck in traditional systems.

Nonetheless, the proposed systems have some limitations. They exhibit marginally lower spectral efficiency compared to other QAM-FBMC systems. Additionally, due to the extended observation window, they experience higher latency compared to conventional QAM-FBMC systems with $K = 4$, and their performance in highly time-selective channels is not guaranteed. Future research directions could include addressing these limitations, developing channel estimation methods, and applying MIMO techniques to further enhance the proposed QAM-FBMC system.

REFERENCES

[1] *Evolved Universal Terrestrial Radio Access (E-UTRA); Physical Channels and Modulation*, Standard (TS) 36.211, v14.2.0, 3GPP Technical Specification, 3rd Generation Partnership Project, Mar. 2017.

[2] *NR: Physical Channels and Modulation*, Standard (TS) 38.211, v15.0.0, 3GPP Technical Specification, 3rd Generation Partnership Project, Dec. 2017.

[3] *IEEE Standard for Information Technology—Telecommunications and Information Exchange Between Systems Local and Metropolitan Area Networks–Specific Requirements—Part 11: Wireless LAN Medium Access Control (MAC) and Physical Layer (PHY) Specifications Amendment 1: Enhancements for High-Efficiency WLAN*, Standard 802.11ax-2021, May 2021.

[4] X. Zhang, L. Chen, J. Qiu, and J. Abdoli, "On the waveform for 5G," *IEEE Commun. Mag.*, vol. 54, no. 11, pp. 74–80, Nov. 2016.

[5] G. Wunder, P. Jung, M. Kasparick, T. Wild, F. Schaich, Y. Chen, S. T. Brink, I. Gaspar, N. Michailow, A. Festag, L. Mendes, N. Cassiau, D. Ktenas, M. Dryjanski, S. Pietrzyk, B. Eged, P. Vago, and F. Wiedmann, "5GNOW: Non-orthogonal, asynchronous waveforms for future mobile applications," *IEEE Commun. Mag.*, vol. 52, no. 2, pp. 97–105, Feb. 2014.

[6] B. Farhang-Boroujeny, "OFDM versus filter bank multicarrier," *IEEE Signal Process. Mag.*, vol. 28, no. 3, pp. 92–112, May 2011.

[7] B. Farhang-Boroujeny and H. Moradi, "OFDM inspired waveforms for 5G," *IEEE Commun. Surveys Tuts.*, vol. 18, no. 4, pp. 2474–2492, 4th Quart., 2016.

[8] S. Mahama, Y. J. Harbi, A. G. Burr, and D. Grace, "Design and convergence analysis of an IIC-based BICM-ID receiver for FBMC-QAM systems," *IEEE Open J. Commun. Soc.*, vol. 1, pp. 563–577, 2020.

[9] M. Morelli, C.-C.-J. Kuo, and M.-O. Pun, "Synchronization techniques for orthogonal frequency division multiple access (OFDMA): A tutorial review," *Proc. IEEE*, vol. 95, no. 7, pp. 1394–1427, Jul. 2007.

[10] R. Zakaria and D. L. Ruyet, "A novel filter-bank multicarrier scheme to mitigate the intrinsic interference: Application to MIMO systems," *IEEE Trans. Wireless Commun.*, vol. 11, no. 3, pp. 1112–1123, Mar. 2012.
[11] C. Kim, K. Kim, Y. H. Yun, Z. Ho, B. Lee, and J.-Y. Seol, "QAM-FBMC: A new multi-carrier system for post-OFDM wireless communications," in *Proc. IEEE Global Commun. Conf. (GLOBECOM)*, San Diego, CA, USA, Dec. 2015, pp. 1–6.
[12] C. Kim, Y. H. Yun, K. Kim, and J.-Y. Seol, "Introduction to QAM-FBMC: From waveform optimization to system design," *IEEE Commun. Mag.*, vol. 54, no. 11, pp. 66–73, Nov. 2016.
[13] H. G. Feichtinger and T. Strohmer, *Gabor Analysis and Algorithms: Theory and Applications*. Boston, MA, USA: Birkhäuser, 1998.
[14] H. Nam, M. Choi, S. Han, C. Kim, S. Choi, and D. Hong, "A new filter-bank multicarrier system with two prototype filters for QAM symbols transmission and reception," *IEEE Trans. Wireless Commun.*, vol. 15, no. 9, pp. 5998–6009, Sep. 2016.
[15] D. Jeon, S. Kim, B. Kwon, H. Lee, and S. Lee, "Prototype filter design for QAM-based filter bank multicarrier system," *Digit. Signal Process.*, vol. 57, pp. 66–78, Oct. 2016.
[16] H. Kim, H. Han, and H. Park, "Waveform design for QAM-FBMC systems," in *Proc. IEEE 18th Int. Workshop Signal Process. Adv. Wireless Commun. (SPAWC)*, Sapporo, Japan, Jul. 2017, pp. 1–5.
[17] I. Galdino, R. Zakaria, D. Le Ruyet, and M. L. R. De Campos, "Prototype filter for QAM-FBMC systems based on discrete prolate spheroidal sequences (DPSS)," *IEEE Access*, vol. 10, pp. 31244–31254, 2022.
[18] H. Han, N. Kim, and H. Park, "Design of QAM-FBMC waveforms considering MMSE receiver," *IEEE Commun. Lett.*, vol. 24, no. 1, pp. 131–135, Jan. 2020.
[19] H. Han, G. Kwon, and H. Park, "MMSE-interference canceling receiver for QAM-FBMC systems," *IEEE Commun. Lett.*, vol. 24, no. 11, pp. 2589–2593, Nov. 2020.
[20] I. Galdino, R. Zakaria, D. L. Ruyet, and M. L. R. de Campos, "Advanced receivers for QAM-FBMC systems with short filters," in *Proc. IEEE Latin-Amer. Conf. Commun. (LATINCOM)*, Rio de Janeiro, Brazil, Nov. 2022, pp. 1–6.
[21] I. G. Andrade, R. Zakaria, D. Le Ruyet, and M. L. R. de Campos, "Short-filter design for intrinsic interference reduction in QAM-FBMC modulation," *IEEE Commun. Lett.*, vol. 24, no. 7, pp. 1487–1491, Jul. 2020.
[22] I. Galdino, D. L. Ruyet, R. Zakaria, and M. L. R. De Campos, "Time-frequency tiling and the BER performance of QAM-FBMC systems with short filters," in *Proc. 17th Int. Symp. Wireless Commun. Syst. (ISWCS)*, Berlin, Germany, Sep. 2021, pp. 1–6.
[23] I. Galdino, R. Zakaria, D. Le Ruyet, and M. de Campos, "Does hexagonal lattice improve the performance of QAM-FBMC?" *J. Commun. Inf. Syst.*, vol. 38, no. 1, pp. 68–76, May 2023.
[24] R. Nissel, S. Schwarz, and M. Rupp, "Filter bank multicarrier modulation schemes for future mobile communications," *IEEE J. Sel. Areas Commun.*, vol. 35, no. 8, pp. 1768–1782, Aug. 2017.
[25] R. Arjun, H. Shah, S. Dhua, P. M. Krishna, K. Appaiah, and V. M. Gadre, "Low complexity FBMC for wireless MIMO systems," *Phys. Commun.*, vol. 47, Aug. 2021, Art. no. 101332.
[26] T. Jang, J. Kim, and J. H. Cho, "A design of spectrally-efficient low-complexity QAM-FBMC systems with mismatched prototype filters," *IEEE Trans. Veh. Technol.*, vol. 71, no. 12, pp. 13043–13059, Dec. 2022.
[27] M. Bellanger. (Jun. 2010). *FBMC Physical Layer: A Primer*. [Online]. Available: http://www.ict-phydyas.org
[28] E. Gutiérrez, J. A. López-Salcedo, and G. Seco-Granados, "Unified framework for flexible multi-carrier communication systems," in *Proc. 8th Int. Workshop Multi-Carrier Syst. Solutions*, Herrsching, Germany, May 2011, pp. 1–5.
[29] Y. H. Yun, C. Kim, K. Kim, Z. Ho, B. Lee, and J.-Y. Seol, "A new waveform enabling enhanced QAM-FBMC systems," in *Proc. IEEE 16th Int. Workshop Signal Process. Adv. Wireless Commun. (SPAWC)*, Stockholm, Sweden, Jun. 2015, pp. 116–120.
[30] H. Nam, M. Choi, C. Kim, D. Hong, and S. Choi, "A new filter-bank multicarrier system for QAM signal transmission and reception," in *Proc. IEEE Int. Conf. Commun. (ICC)*, Sydney, NSW, Australia, Jun. 2014, pp. 5227–5232.
[31] U. Madhow and M. L. Honig, "MMSE interference suppression for direct-sequence spread-spectrum CDMA," *IEEE Trans. Commun.*, vol. 42, no. 12, pp. 3178–3188, Dec. 1994.
[32] S. Mirabbasi and K. Martin, "Overlapped complex-modulated transmultiplexer filters with simplified design and superior stopbands," *IEEE Trans. Circuits Syst. II, Analog Digit. Signal Process.*, vol. 50, no. 8, pp. 456–469, Aug. 2003.
[33] R. Yavne, "An economical method for calculating the discrete Fourier transform," in *Proc. Fall Joint Comput. Conf., I (AFIPS)*, New York, NY, USA, Dec. 1968, pp. 115–125.
[34] W. A. Gardner, *Cyclostationarity in Communications and Signal Processing*. Piscataway, NJ, USA: IEEE Press, 1994.
[35] H. Ochiai, "An analysis of band-limited communication systems from amplifier efficiency and distortion perspective," *IEEE Trans. Commun.*, vol. 61, no. 4, pp. 1460–1472, Apr. 2013.
[36] *Evolved Universal Terrestrial Radio Access (E-UTRA); Base Station (BS) Radio Transmission and Reception*, Standard (TS) 36.104, v17.2.0, 3GPP Technical Specification, 3rd Generation Partnership Project, Jun. 2021.
[37] *Deployment Aspects*, Standard (TR) 25.943, v16.0.0, 3GPP Technical Report, 3rd Generation Partnership Project, Jun. 2020.

TAEJUN JANG received the B.S. and M.S. degrees in electrical engineering from the Pohang University of Science and Technology (POSTECH), Pohang, South Korea, in 2015 and 2017, respectively, where he is currently pursuing the Ph.D. degree. His research interests include waveform design and mobile communications.

JOON HO CHO (Member, IEEE) received the B.S. degree (summa cum laude) in electrical engineering from Seoul National University, Seoul, South Korea, in 1995, and the M.S.E.E. and Ph.D. degrees in electrical and computer engineering from Purdue University, West Lafayette, IN, USA, in 1997 and 2001, respectively.

From 2001 to 2004, he was an Assistant Professor with the University of Massachusetts at Amherst. Since 2004, he has been with the Pohang University of Science and Technology (POSTECH), where he is currently an Associate Professor with the Department of Electrical Engineering. His research interests include waveform design, multiuser communications, MIMO signal processing, channel measurement and modeling, and information theory.

Dr. Cho served as an Associate Editor for IEEE TRANSACTIONS ON VEHICULAR TECHNOLOGY and served as the Vice President for Admissions and Student Affairs of POSTECH.